

Malate-Based Biodegradable Scaffolds Activate Cellular Energetic Metabolism for Accelerated Wound Healing

Min Wu,[§] Yitao Zhao,[§] Meihan Tao, Meimei Fu, Yue Wang, Qi Liu, Zhihui Lu, and Jinshan Guo^{*§}



Cite This: *ACS Appl. Mater. Interfaces* 2023, 15, 50836–50853



Read Online

ACCESS |



Metrics & More



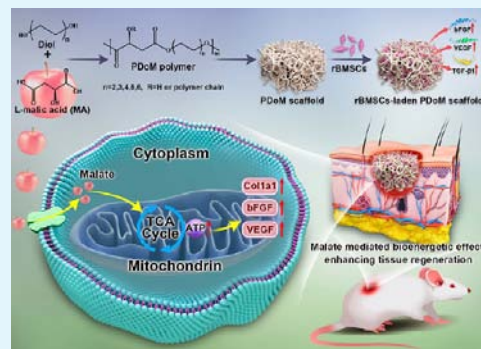
Article Recommendations



Supporting Information

ABSTRACT: The latest advancements in cellular bioenergetics have revealed the potential of transferring chemical energy to biological energy for therapeutic applications. Despite efforts, a three-dimensional (3D) scaffold that can induce long-term bioenergetic effects and facilitate tissue regeneration remains a big challenge. Herein, the cellular energetic metabolism promotion ability of L-malate, an important intermediate of the tricarboxylic acid (TCA) cycle, was proved, and a series of bioenergetic porous scaffolds were fabricated by synthesizing poly(diols L-malate) (PDoM) prepolymers via a facial one-pot polycondensation of L-malic acid and aliphatic diols, followed by scaffold fabrication and thermal-cross-linking. The degradation products of the developed PDoM scaffolds can regulate the metabolic microenvironment by entering mitochondria and participating in the TCA cycle to elevate intracellular adenosine triphosphate (ATP) levels, thus promoting the cellular biosynthesis, including the production of collagen type I (Col1a1), fibronectin 1 (Fn1), and actin alpha 2 (Acta2/ α -Sma). The porous PDoM scaffold was demonstrated to support the growth of the cocultured mesenchymal stem cells (MSCs) and promote their secretion of bioactive molecules [such as vascular endothelial growth factor (VEGF), transforming growth factor- β 1 (TGF- β 1), and basic fibroblast growth factor (bFGF)], and this stem cells-laden scaffold architecture was proved to accelerate wound healing in a critical full-thickness skin defect model on rats.

KEYWORDS: malate, energy metabolism, biosynthesis, elastomer, wound healing



1. INTRODUCTION

Efforts to dissolve unmet requirements in biomedical engineering impels the progress of regenerative medicine. As the largest organ in the human body, skin tissue regeneration is one of the research hotspots and large-scale skin grafting cases performed worldwide each year, aiming to address the clinical needs of repairing skin damage caused by surgery, acute trauma, burns, or chronic wounds.^{1–3} However, there are some limitations of skin grafting, including donor site shortage, donor site scar, and the risk of infection.² Tissue engineered skin provides a new treatment concept for acute or chronic skin injuries.³ Tissue engineering establishes a three-dimensional (3D) complex of cells and biomaterial scaffolds to restore the morphology, structure, and function of the defect tissue,⁴ especially in solving the problem of the origin of transplanted tissue, which can reduce the overdependence on transplanted tissue. Although the development of biomaterials has made considerable improvement, existing materials do not yet meet the requirements for accurate biomimetic tissue repair and often lack the necessary biological cues to mediate complex tissue repair.^{5–7} Hence, a comprehensive understanding of the microenvironmental factors associated with tissue repair, containing the interaction of secreted factors, extracellular matrix, chemical, and physical stimuli,^{8,9} is essential for material design that guides stem cells and other

repair cells to maximize their potency to improve therapeutic outcomes. Focusing on metabolic factors in the microenvironment of repair cells, bioenergetic cues including glutamine,^{10,11} glucose,¹² citrate,¹³ and phosphates,^{13,14} showing significant roles in cell proliferation and differentiation.

Cellular activities are highly dependent on an adequate energetic supply,¹⁵ energy metabolism provides energy substances such as adenosine triphosphate (ATP) and substrates for the rapid biosynthesis of macromolecules required for cell growth, proliferation, and differentiation.¹⁶ It has been suggested that enhancing energy metabolism could help enhance the ability to tissue repair.^{17–20} At present, the research on energy metabolism bioenergetic materials mainly focuses on tricarboxylic acid (TCA) metabolism regulating materials. Yang et al. demonstrated that in the osteogenic differentiation process of mesenchymal stem cells (MSCs), exogenous citrate uptake by MSCs can significantly promote the osteogenic differentiation and mineralization by elevating

Received: June 29, 2023

Revised: October 8, 2023

Accepted: October 15, 2023

Published: October 30, 2023



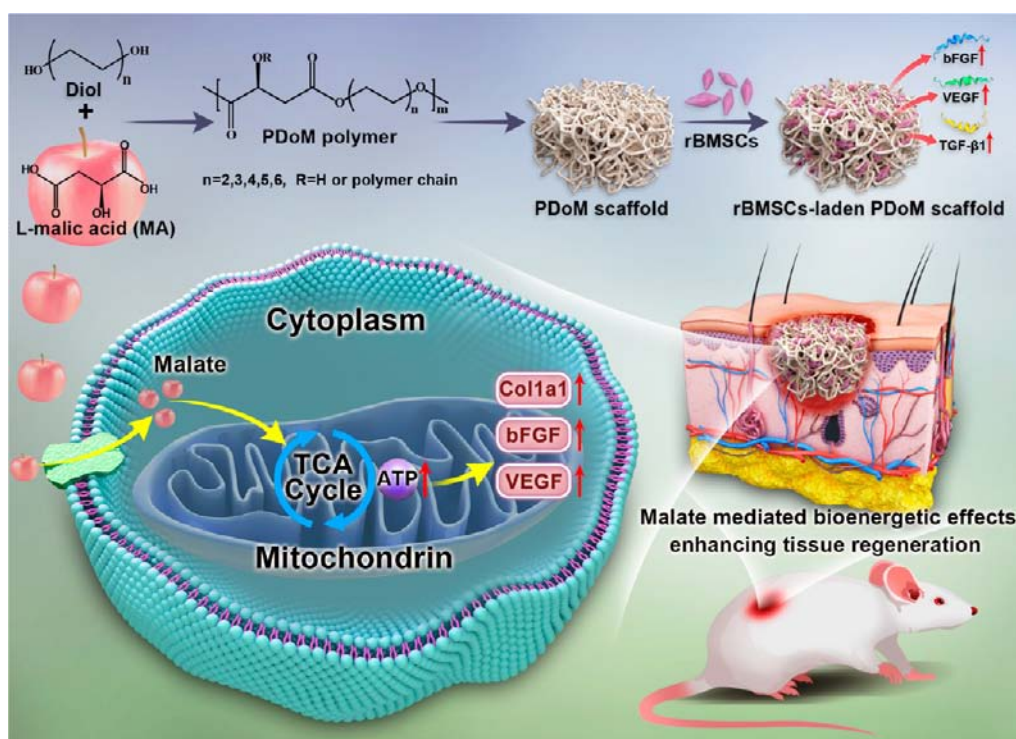


Figure 1. Synthesis of PDoM and the fabrication of rBMSC-laden PDoM scaffold for accelerated wound healing in a critical full-thickness skin defect model on rats and the potential mechanism of the degraded malate in ameliorating the bioenergetic metabolic microenvironment by entering in the TCA cycle and elevating ATP production and the following biosynthesis, especially wound healing-related proteins.

the energy metabolism level of MSCs through TCA metabolism regulation.¹³ Zhang et al. found that the degraded molecular fragments of succinate-based scaffold directly participate in mitochondrial TCA metabolism or establish metabolic bypasses and thus can enhance cellular energy metabolism in situ, significantly promoting bone regeneration.²¹ However, up to now, there has been no report about the construction of bioenergetic materials using malate, a metabolic intermediate. As a crucial intermediate metabolite in the TCA cycle, malate is also the main component of the malate-aspartate shuttle. Emerging studies demonstrate that, in the process of osteogenic differentiation, glucose's entry into mitochondria serves an important role in producing malate, catalyzed by mitochondrial malic enzyme (Me2). The resulting malate then proceeds into the cytoplasm using the malate-aspartate shuttle mechanism to replenish nicotinamide adenine dinucleotide (NAD⁺) and maintain glycolysis,²² implying that malate is involved in not only TCA metabolism but also glycolysis. Therefore, the incorporation of malate into biomaterials could potentially be highly effective at boosting energy metabolism during tissue repair.

Herein, we proved that exogenous *L*-malate could accelerate cellular energy metabolism, which can further promote the following biosynthesis. Inspired by this, via a facile polycondensation of *L*-malic acid and aliphatic diols, followed by scaffold fabrication and thermal cross-linking, a bioenergetic poly(diols *L*-malate) (PDoM) scaffold was developed. We hypothesized that, with the continuous degradation, the released *L*-malate and *L*-malate-containing fragments can enter cells to modulate cell energy metabolism, specifically, boosting cellular energy levels by actively participate in the TCA cycle via entering the mitochondria to regulate the metabolic microenvironment thus to promote wound healing

(Figure 1). Furthermore, the PDoM scaffold could support the growth of the cocultured MSCs and promote their secretion of bioactive molecules which would potentially be conveyed via the pores of the PDoM scaffold directly to the site of the targeted defective tissue for accelerating tissue regeneration.

2. MATERIALS AND METHODS

2.1. Materials. *L*-Malic acid (MA), 1,4-butanediol (BD), 1,6-hexanediol (HD), 1,8-octanediol (OD), 1,10-decanediol (DD), and 1,12-dodecanediol (DDD) were obtained from Aladdin Biological Technology Co., Ltd. (Shanghai, China). Citric acid (CA) was purchased from Sigma-Aldrich. 1,4-dioxane, acetone, diiodomethane, and dimethyl sulfoxide-*d*₆ (DMSO-*d*₆) were purchased from Merck CO., Ltd. (Shanghai, China). The chemicals were used as received without purification.

2.2. Synthesis of PDoM. MA was reacted with BD, HD, OD, DD, or DDD to synthesize a PDoM prepolymer first, which was then thermal cross-linked to give a PDoM elastomer. Representatively, the synthesis of a poly(1,8-octanediol *L*-malate) (POM) prepolymer was presented here. Briefly, 26.8 g of MA (0.20 mol) and 29.2 g of OD (0.20 mol) were charged into a 250 mL round-bottom flask containing a magnetic stir bar. The mixture was melted by heating it to 140 °C under an oil bath while being stirred, and the reaction was sustained at 120 °C until the speed of the stir bar decreased to 60 rpm. Thus-obtained crude prepolymer was dissolved in 150 mL of 1,4-dioxane, and then, the prepolymer was precipitated in deionized (DI) water and further washed thoroughly with DI water at least three times before free-drying to give POM-1.0 (1.0 representing the ratio between MA and OD) prepolymer. The synthesis of POM-1.2, POM-1.5, and POM-2.0 prepolymers were conducted according to the same procedure described in the synthesis of POM-1.0 prepolymer. The molar ratios of MA: OD = 1.2:1.0, 1.5:1.0, and 2.0:1.0 for POM-1.2, POM-1.5, and POM-2.0 prepolymers, respectively. Poly(1,4-butanediol *L*-malate) (PBM), poly(1,6-hexanediol *L*-malate) (PHM), poly(1,10-decanediol *L*-malate) (PDM), and poly(1,12-dodecanediol *L*-malate) (PDDM) prepolymers were also synthesized following a

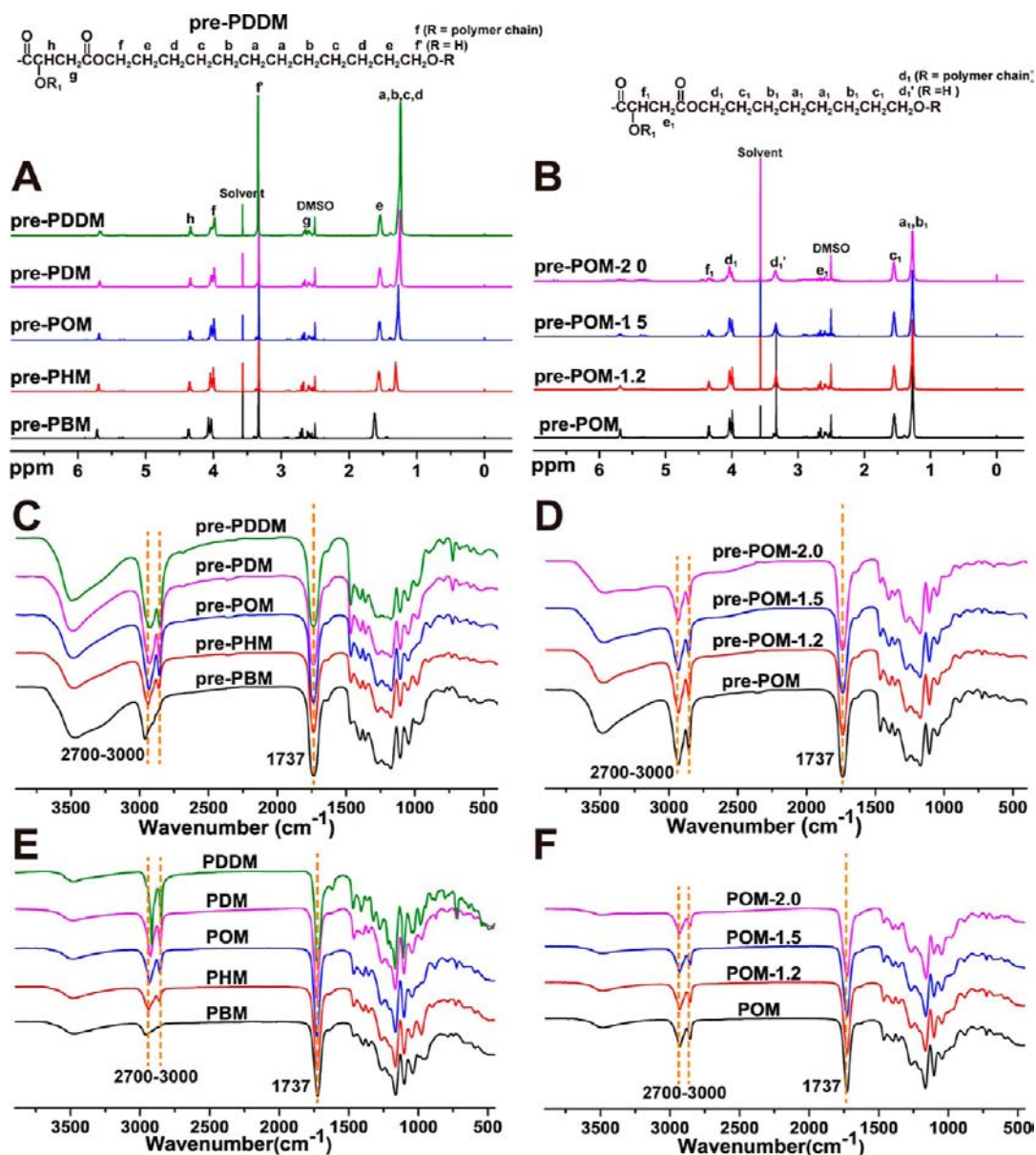


Figure 2. Characterizations of PDoM: ^1H NMR (A,B) and FTIR (C,D) spectra of PDoM prepolymers synthesized via one-pot polycondensation reaction between aliphatic diols with different chain lengths and L-malic acid (MA) using different MA/diol ratios; ATR-FTIR spectra (E,F) of cross-linked PDoM polymers (120°C , 3 days, plus 120°C under vacuum for another 3 days).

similar procedure as that of the POM-1.0 prepolymer, and the ratios between MA and these diols used were all kept as 1.0:1.0.

For the postpolymerization, the POM-1.0 prepolymer solution in 1,4-dioxane (30 wt %) was cast in a Teflon dish and the solvent was allowed to evaporate; then, the casted prepolymer was thermally cross-linked at either 110 , 120 , or 130°C for 3 days, followed by 120°C under vacuum for 1–3 days to give cross-linked POM-1.0 with various cross-linking degrees. For comparison, all prepolymers of POM-1.2, POM-1.5, POM-2.0, PBM-1.0, PHM-1.0, PDM-1.0, and PDDM-1.0 were uniformly subjected to a thermal cross-linking condition of 120°C for 3 days, followed by additional 3 days at 120°C under vacuum.

2.3. Characterizations of PDoM. The proton nuclear magnetic resonance (^1H NMR) spectra of prepolymers were obtained using an AVANCE IIIITM HD 600 MHz spectrometer in $\text{DMSO}-d_6$. The results are listed in Figure 2. Representative peaks of ^1H NMR (600 MHz; $\text{DMSO}-d_6$; δ , ppm) for pre-POM: 1.27 (s, $-\text{OCH}_2\text{CH}_2(\text{CH}_2)_4-$ from OD), 1.55 (s, $-\text{OCH}_2\text{CH}_2-$ from OD), 2.53–2.69 (m, $-\text{CH}(\text{OH})-\text{CH}_2-\text{CO}-$ from MA), 3.57 (br, $-\text{CH}_2-$

OH from OD), 3.98–4.04 (br, $-\text{COOCH}_2-$ from OD), 4.35 (br, $-\text{OCO}-\text{CH}(\text{OH})-$ from MA), 5.69 (br, $-\text{OCO}-\text{CH}(\text{OCO})-\text{CH}_2-$ from MA).

The Fourier transform infrared (FTIR) spectra of PDoM prepolymers were obtained using a Thermo Fisher Scientific Nicolet iS50 FTIR spectrometer, the prepolymer solutions in acetone were cast on KBr slices and dried overnight before measurement. The attenuated total reflectance-FTIR (ATR-FTIR) spectra of PDoM polymers (120°C , 3 days and 120°C , vacuum, 3 days) were conducted using the cross-linked polymer films directly, measured by a Thermo Scientific Nicolet-iS10 FTIR spectrometer with air as the background.

The thermal properties of the cross-linked polymer films were characterized by differential scanning calorimetry (DSC, $-60 \sim 150^\circ\text{C}$) and thermogravimetric analysis (TGA, $20 \sim 800^\circ\text{C}$) at a heating/cooling rate of $10^\circ\text{C}/\text{min}$ under a nitrogen atmosphere. The glass transition temperature (T_g) was identified by determining the midpoint of the step change in heat capacity during the initial heating cycle recorded by DSC. For PDDM, a melting peak was detected

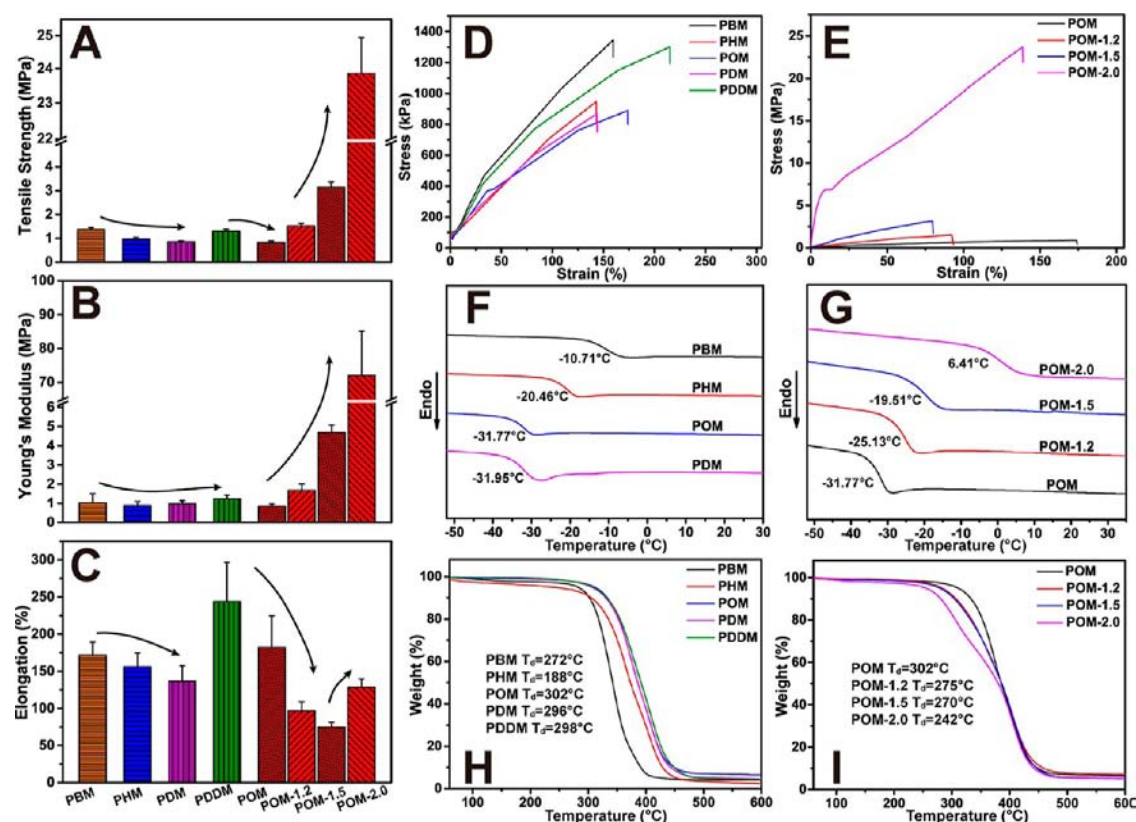


Figure 3. Characterizations of the PDoM polymer films: tensile strengths (A), Young's moduli (B), and elongations at break (C) of cross-linked films of PBM, PHM, POM, PDM, PDDM, POM-1.2, POM-1.5, and POM-2.0 (all cross-linked at 120 °C, 3d plus 120 °C, vacuum, 3d) ($n = 8$); representative stress–strain curves of PBM, PHM, POM, PDM, and PDDM (D) as well as POM with different MA/OD ratios (E) ($n = 8$); and DSC (F,G) and TGA (H,I) curves of PDoM polymers.

(Figure S1), showing a melting temperature ~ 17 °C. The decomposition temperature (T_d) is defined as the temperature at which 5% weight reduction of the sample is observed from the TGA curve.

Tensile mechanical tests of cross-linked polymer films were carried out with a mechanical tester (AMETEK LS1) outfitted with a load cell capable of measuring up to 500 N. In brief, a rectangular-shaped specimen ($26 \times 4 \times 1.5$ mm, length \times width \times thickness) was subjected to tension at a speed of 500 mm/min until it fractured. From the provided data, stress–strain curves were derived, and the Young's modulus was calculated through determining the initial slope (slope in the 0–10% range) of the stress–strain curve. Each sample was assessed by measuring at least eight specimens, and the average of the results was calculated. The wet mechanical characteristics of the cross-linked films were assessed by immersing them in phosphate-buffered saline (PBS) with a pH of 7.4 for 24 h and measuring their performance under a 500 N load cell until there was no further increase in hydrated weight. The results are shown in Figures 3, S2, and S3 and Table S1.

The cross-linking density (N) of the elastomer was calculated in accordance with the theory of rubber elasticity, as described by eq 1²³

$$N = \frac{E_0}{3RT} = \frac{\rho}{M_c} \quad (1)$$

where N refers to the number of active network chain segments per unit volume (mol/m^3); M_c represents the molecular weight between cross-links (g/mol); E_0 represents Young's modulus (Pa); R is the universal gas constant ($8.3144 \text{ J}/\text{mol}\cdot\text{K}$); T is the absolute temperature (K); and ρ is the elastomer density (g/m^3) measured by a Mettler Toledo balance according to Archimedes' principle, with the assistance of DI water.

The contact angles (10 s after water dropping) of cross-linked PDoM films were determined by means of the sessile drop method²⁴ at room temperature by Drop Shape Analysis System (SL250/SL150). The measurement was conducted using DI water and diiodomethane. Matlab software was utilized to calculate the surface energy via the Harmonic mean equations,²⁵ and the results are shown in Table S2. The results for each sample were determined from four unrelated measurements conducted at varied locations and subsequently averaged. The evolution of water-in-air contact angles on the surface of the films was tracked for a period of 30 min following water droplet deposition. The results are presented in Figures S4 and Table S2.

2.4. In Vitro and In Vivo Degradation Study. For in vitro degradation, disk-shaped polymer films (7 mm in diameter and 0.3–0.5 mm in thickness) were transferred into tubes filled with either 10 mL of PBS (pH 7.4) or a 0.1 M NaOH solution and incubated at 37 °C to determine the relative degradation rates between different samples. At preset time points, samples were subjected to over three washes using DI water to eliminate any potential salt residue, followed by a week-long freeze-drying process. The proportionate mass loss (%) was evaluated using eq 2, which involves contrasting the starting mass (W_0) with the weight measured at a particular time (W_t). Five duplicate measurements were taken for each sample, and the results are presented as mean values with the corresponding standard deviations.

$$\text{Mass loss (\%)} = \frac{W_0 - W_t}{W_0} \times 100 \quad (2)$$

For in vivo degradation, disk-shaped polymer films of PBM, POM, PDDM, POM-1.5, and poly(lactic-co-glycolic acid) (PLGA, LA/GA = 50/50, Mw ~ 30 kDa, from Guangzhou Boqiang Biotechnology Ltd.) samples (7 mm in diameter, 0.5–0.7 mm in thickness) were

subcutaneously implanted under the skin in the backs of healthy, 3 month-old female Sprague–Dawley (SD) rats after undergoing sterilization with 70% ethanol, sterile PBS (pH 7.4), and UV light in the order; the samples were left to dry overnight in a cell culture hood. Each sample was subjected to three tests using different specimens. At the end of 1, 4, and 12 weeks, the specimens were collected, rinsed with PBS and DI water, and then subjected to freeze-drying. Weight loss was calculated using eq 2.

2.5. Cell Culture and Medium. Mouse fibroblasts (L929) were incubated in complete Dulbecco's modified Eagle's medium (DMEM, Gibco, Thermo Fisher Scientific, USA), with 10% (v/v) fetal bovine serum (FBS, VivaCell Biosciences, China) and 1% (v/v) penicillin–streptomycin (Gibco, USA). Rat bone mesenchymal stem cells (rBMSCs, Cyagen RASM-X-01001, passages 4–6) were cultured in α -Minimal Essential Medium (α -MEM) added with 10% FBS and 1% penicillin–streptomycin. The cultured cells were grown in a moist incubator under a 5% CO₂ atmosphere at 37 °C.

2.6. Cytotoxicity and Proliferation Study. The cytocompatibility of cross-linked PDoM polymers was evaluated utilizing a Cell Counting Kit-8 (CCK-8) assay against L929, with PLGA and poly(1,8-octanediol citrate) (POC, synthesized according to earlier literatures)^{26,27} as controls. Equal weight (1.0 g) of cross-linked PDoM (PBM, PHM, POM, POM-1.2, POM-1.5, POM-2.0, PDM, and PDDM) films were completely degraded in a 10 mL 0.2 M NaOH solution, and the resulting solutions were subsequently diluted into three different dilutions [1×, 10× and 100×, 1× means the undiluted solution; 10× and 100× represent 10- and 100-fold dilutions by sterile PBS (pH 7.4) of the 1× solution, respectively]. The solutions mentioned above were neutralized to a pH of 7.4 and passed through a 0.22 μ m membrane filter before being utilized in the cell culture. Subsequently, 200 μ L of L929 suspension in complete DMEM medium with a cell concentration of 5×10^4 cells/mL was added to each well of a 96-well cell culture plate and incubated for 24 h at 37 °C, 5% CO₂, and 95% relative humidity. Next, 20 μ L of 1×, 10×, or 100× degradation products was added and the cells were further cultured for an additional 24 h, followed by CCK-8 assay analysis as per the manufacturer's protocol.

The cell proliferation of L929 treated with 10× degradation products was also evaluated by the CCK-8 assay after incubating for 1, 3, and 5 days using PLGA and POC as controls. Briefly, cell detachment was carried out followed by suspension in media to achieve a seeding density of 1×10^4 cells/mL. Subsequently, 200 μ L of the cell suspension was dispensed into each well of 96-well plates and allowed to incubate for 24 h; then, 20 μ L of a 10× degradation product was added to each well, and the cell amounts were measured at 1, 3, and 5 days using the CCK-8 assay.

The rBMSCs with 4–6 passages were used for cell culture experiments. To evaluate the impact of malate on cell proliferation, cells reaching ~80% confluency were exposed to α -MEM medium containing L-malate (pH-adjusted to 7.4) at various concentrations ranging from 0 to 5,000 μ M and cultured for another 24 h, followed by CCK-8 assay tests. The cell proliferation profile of rBMSCs cocultured with 10× degradation products of different polymers was assessed using CCK-8 assay and Live/Dead staining after incubating for 1, 3, and 5 days, with PLGA and POC as controls. Briefly, to a well of a 96-well plate containing ~80% confluent rBMSCs and 200 μ L of medium, 20 μ L of 10× degradation product was added, and the cells were cultured for determined periods before the CCK-8 assay test. For the Live/Dead assay, rBMSCs were seeded at a density of 5×10^4 cells/cm² into 12-well plates (5000 cells/well) and then cultured in 1 mL complete α -MEM medium at 37 °C under 5% CO₂ and 95% relative humidity for 1 day. Subsequently, 100 μ L of 10× degradation product of different polymers was added to each well and incubated for 1, 3, and 5 days. Then, the cell morphology and spreading were examined by Live/Dead staining using an inverted light microscope (Leica, Germany).

2.7. Cell Migration Assay. To assess the effect of polymers on cells' migration, in vitro scratch assay and transwell assay were conducted using POM-1.5 as the representative polymer and L929 as the cell model, with PLGA and POC as controls. The effect of 200

and 2000 μ M MA solutions on cell migration was also studied. For the scratch assay, briefly, L929 cells were seeded in six-well plates at a density of 5×10^4 cells/cm² and cultured in a complete DMEM medium under conditions of 37 °C, 5% CO₂, and 95% relative humidity. Once reaching 80% confluence, the medium was changed with FBS-free DMEM and the cells were cultured for another 24 h before the creation of ~0.5 mm scratches upon the cellular monolayer using a sterile pipet tip. Following that, sterile PBS was utilized for washing the wells to eliminate debris and detached cells, and then, the cells were cultured in 2 mL of FBS-free DMEM. Next, 200 μ L of FBS-free DMEM solutions containing MA monomer or 10× degradation product of POM-1.5 were added to each well, and the cells were further cultured. The scratch area was observed after 0, 24, and 48 h. The percentage of cell migration rate was determined by measuring scratch areas by ImageJ software and calculating the ratio of healing area to initial gap area using eq 3^{28,29}

$$\text{cell migration rate (\%)} = \frac{\text{scratch area (0 h)} - \text{scratch area (24 h)}}{\text{scratch area (0 h)}} \times 100 \quad (3)$$

The transwell experiment was also carried out in accordance with the manufacturer's instructions. In brief, in each well of a transwell (Corning Inc., NY, USA), 1×10^4 L929 cells were seeded on the upper chamber with 100 μ L of serum-free DMEM. Following this, the lower layer was supplemented with 500 μ L of DMEM containing either MA monomer or 10× polymer degradation product along with 10% FBS. After 24 h' of culturing, L929 cells on the upper chamber's permeable membrane were fixed using 4% paraformaldehyde and subsequently stained with crystal violet. After that, the membrane was rinsed with sterile PBS thrice and wiped off to eliminate nonmigrated cells. Ultimately, the migrated cells on the lower surface of the membrane were observed using an optical microscope.

2.8. Effect of PDoM to Cells' Biosynthesis. The effect of PDoM and malate on Cells' biosynthesis was assessed using 200 and 2000 μ M MA solutions, POM-1.5 (as the representative polymer), using both L929 and rBMSCs as the cell models, with PLGA and POC as controls. For L929, briefly, cells were seeded in 24-well dishes and cultured in a complete DMEM medium under conditions of 37 °C, 5% CO₂ and 95% relative humidity. To a well of a 24-well plate containing ~80% confluent cells and 500 μ L of medium, 50 μ L of MA solutions or 10× degradation product of POM-1.5 [a solution of 1.0 g in 10 mL of 0.5 M NaOH was neutralized and further diluted by 10 times with PBS (pH 7.4)] were added, and the cells were further cultured for 24 h. The cells treated with 10× degradation products of POC, PLGA and cells without treatment (blank) were used as controls. After that, the cells were collected and lysed. The expression of tissue-specific wound healing related genes, including type-I collagen (Col1a1), fibronectin 1 (Fn1), and actin alpha 2 (Acta2/ α -Sma), was determined by a real-time quantitative polymerase chain reaction (RT-qPCR) assay. The total ribonucleic acid (RNA) was extracted from the cells utilizing the Trizol reagent (TransGen Biotech, Beijing), and the RNA was then converted into complementary DNA (cDNA) by a cDNA Reverse Transcription Kit (TransGen Biotech, Beijing). Finally, a Q-PCR instrument (TransGen Biotech, Beijing) was used for RT-PCR analysis with the housekeeping gene glyceraldehyde-3-phosphate dehydrogenase (GAPDH). Primer sequences are listed in Table S3.

Similarly, rBMSCs were seeded in 24-well dishes and cultured in α -MEM medium under conditions of 37 °C, 5% CO₂ and 95% relative humidity. Then, to 500 μ L of cell culture medium containing ~80% confluent cells, 50 μ L of sterile MA solution in PBS (200 or 2000 μ M) or 10× degradation product of POM-1.5, PLGA, or POC was added, and the cells were cultured for another 24 h. Then, the cells were collected and lysed to determine the expression levels of inflammatory, angiogenic, and growth factor related genes, including interleukin-1 β (IL-1 β), tumor necrosis factor- α (TNF- α), platelet endothelial cell adhesion molecule-1 (CD31), vascular endothelial growth factor (VEGF), transforming growth factor- β 1 (TGF- β 1), and basic fibroblast growth factor (bFGF), by RT-qPCR. The cell culture

supernatants were also collected for enzyme-linked immunosorbent assay (ELISA) testing to determine the levels of IL-1 β , VEGF, and bFGF, following the manufacturer's guidelines (Jiangsu Meimian Industrial Co., Ltd., Jiangsu, China).

2.9. Effect of PDoM to Cells' Energy Metabolism. The effect of PDoM and malate on the cells' energy metabolism was assessed using 200 and 2000 μ M MA solutions, POM-1.5 (as the representative polymer), with PLGA and POC as controls. For intracellular ATP level study, L929 or rBMSCs were seeded into 12-well plates at a density of 5×10^4 cells/cm² and then, cultured in 1 mL of complete medium at 37 °C, 5% CO₂, and 95% relative humidity. Once reaching 80% confluence, 100 μ L of MA solution or 10 \times polymer degradation product was added and the cells were incubated for another 24 h. The cells treated with 10 \times degradation solutions of POC, PLGA, and cells without treatment (blank) were used as controls. Then, the cell culture media were removed, and an ATP assay kit (Beyotime) was used to quantify the level of intracellular ATP. As a primary chemical driver of ATP production, the effect of polymer degradation product to the mitochondrial membrane potential ($\Delta\psi$ m) was also studied using a mitochondrial membrane potential assay kit (JC-1), a cationic indicator for $\Delta\psi$ m, to assess the cells' oxidative metabolism.

For rBMSCs, to investigate the effect of malate-based polymer and malate to the key transport proteins participating in the TCA cycle, including [isocitrate dehydrogenase (IDH-3), succinate dehydrogenase (SDH), and malate dehydrogenase (MDH)], the gene expression levels of them during the energy metabolism regulation process of cells after being treated with MA monomer or 10 \times polymer degradation solutions for 24 h were analyzed by the RT-qPCR assay. Ultraperformance liquid chromatography-tandem mass spectrometry (UPLC-MS/MS) was also utilized to detect the critical energy metabolites. After coculture with the MA solution, or 10 \times polymer degradation product of POM-1.5 for 24 h, the rBMSCs (1×10^7 cells/cm²) were washed with PBS and then mixed with 1 mL of cold methanol: acetonitrile: water (2:2:1, v/v/v) to extract intracellular metabolites. After being kept on ice, the samples were sonicated for an hour and then subjected to centrifugation at 16,000g at 4 °C for 20 min. The supernatant was used for subsequent UPLC-MS/MS analysis. The UPLC-MS/MS analysis involved the use of a Nexera X2 LC-30AD UHPLC system (Shimadzu, Kyoto, Japan) in conjunction with a 5500 QTRAP mass spectrometer (AB SCIEX, Toronto, Canada). For LC, (A) aqueous acetonitrile (v/v) at 5% and (B) aqueous acetonitrile (v/v) at 95% made up the mobile phase. The mass spectrometer was set to negative ionization and multiple reaction monitoring modes. The metabolomics data were processed with MultiQuant software (AB SCIEX, Toronto, Canada). All sample peaks were detected and aligned with respect to their corresponding standard substances (Sigma-Aldrich).

2.10. In Vivo Foreign Body Response. To assess the in vivo compatibility and inflammatory response of the cross-linked PDoM films, PBM, POM, PDDM, and POM-1.5 were chosen as the representatives to conduct foreign body response study by subcutaneously implanting the films on the back of SD rats using PLGA films with the same thickness as control. All animal studies were conducted following the protocol approved (Approval no. SMUL2022064) by The Institutional Animal Care Committee of Southern Medical University (Guangzhou, China). Briefly, following the sterilization and drying process carried out in the cell-culture hood according to the method described above, disk-shaped films (7 mm in diameter, 0.5–0.7 mm in thickness) were subcutaneously implanted in the superior (upper) or inferior (lower) part of the back of healthy female SD rats (3 months old). Twelve SD rats were randomly separated into three groups with four rats per group. For each SD rat, four specimens of different samples were implanted. At each of the three preset time points (1, 4, and 12 weeks), four rats were euthanized using excessive CO₂ exposure, and the polymer films with adjacent tissues were harvested and preserved by immersing them in 4% paraformaldehyde. The automated tissue processor was utilized to process the specimens, which were then embedded in paraffin wax and sliced into 4 μ m sections. For each sample, six tissue sections

from different regions were examined using hematoxylin and eosin (H & E) staining. In order to determine the existence of inflammatory cells, CD11b (an inflammatory cell marker) staining was also conducted using another six slides for each sample. The numbers of cells within a portion of the skin-side tissue measuring $200 \times 200 \mu$ m² adjacent to the implanted polymer films was determined through quantitative analysis using H & E staining images by ImageJ. At least eight square regions from different specimens were studied for each sample, and the results were averaged to obtain a representative value. Similarly, the process for counting the CD11b⁺ cells in the CD11b immunohistochemically stained specimens was consistent with that of the previous method, but only CD11b positively stained cells were counted.

2.11. Scaffold Fabrication. Pre-POM-1.5 was chosen as the representative prepolymer to fabricate porous scaffold following the process reported in our previous literature.^{30,31} Briefly, 10.0 g 30 wt % pre-POM-1.5 solution in 1,4-dioxane and 12.0 g (porosity: 80 wt %) sieved salt (125–200 μ m, as porogen) were uniformly mixed, and the solvent was continually evaporated under a chemical hood. After being cast into square-shaped poly(tetrafluoroethylene) (PTFE, Teflon) molds, the resultant slurry was then cross-linked at 120 °C for 3 days and then remained under vacuum at the same temperature for an additional 3 days. After that, the scaffolds underwent a process of salt leaching by washing them with DI water for a duration of more than 1 week; DI water was changed every other day, until all salt was removed. After freeze-drying, the scaffolds were obtained and subsequently stored in a vacuum desiccator before use. The morphologies of scaffolds and cells grown on scaffolds were observed by scanning electron microscopy (SEM, Zeiss Sigma 300).

2.12. BMSCs Cocultured on Scaffold. POM-1.5 scaffolds were shaped into circular discs with a 16 mm diameter suitable for 24-well plates using a die-cutting method. Prior to cell seeding, the scaffold disks were subjected to sterilization through a series of steps including treatment with 75% ethanol, sterile PBS (pH 7.4), and exposure to UV light, before being placed in DMEM. Afterward, rBMSCs in a complete α -MEM medium were seeded on the scaffolds in the wells of a 24-well plate with 500 μ L of medium per well, and the cells were incubated for 5 days with medium changes every other day. The morphology and spreading of rBMSCs on the POM-1.5 scaffold on day 5 were further observed by SEM after fixing the cells using a 2.5% (w/v) glutaraldehyde solution in PBS followed with gradient dehydration and air-drying.

2.13. In Vivo Wound Healing Study. A full-thickness cutaneous wound model was created on SD rats to evaluate the wound healing efficacy of malate-based bioenergetic scaffold, using POM-1.5 and POM-1.5 + BMSC as the representatives, with Tegaderm film (3 M Tegaderm Dressings)-treated wounds and untreated wounds as controls. All animal experiments were performed according to protocols approved by the Institutional Animal Care Committee of Southern Medical University (Guangzhou, China) (Approval no. SMUL2022064). Briefly, a total of 12 male SD rats weighing between 200 and 250 g were randomly assigned to four groups (untreated, Tegaderm, POM-1.5, POM-1.5+BMSCs), with four rats in each group. Once the rats were anesthetized with pentobarbital (2 wt %, 2 mL/kg), their back areas were entirely depilated, and four full-thickness wounds (2.0 cm \times 2.0 cm) were produced on each rat's back. An untreated wound was set as a control on every rat. To track the healing progress over time, digital photographs were taken 0, 3, 5, 7, 10, 14, 17, and 21 days post wound treatment. A ruler was situated adjacent to the wound to act as a reference for assessing the wound's size. On each time point of day 7, 14, and 21, four rats were sacrificed and the entire wound along with the surrounding healthy skin was harvested and then fixed in 4% buffered paraformaldehyde and embedded in paraffin blocks for sectioning into 3–5 μ m slices using a microtome. Then, H & E staining and Masson's trichrome staining were conducted to assess the inflammatory response and collagen deposition in the process of wound healing. IL-1 β and VEGF immunohistochemical and CD31 immunofluorescence staining experiments were also conducted to further study the inflammation and vascularization during the wound healing process. All the stained

slices were observed using a positive microscope (Leica DM4000 B, Germany).

2.14. Statistical Analysis. Statistical analysis was performed to all experimental data, with the results reported as the mean \pm standard deviation (SD), and the statistical difference was determined by *t*-test or one-way ANOVA. All the data are considered to have significant differences only when $p < 0.05$. * and ** represent $p < 0.05$ and $p < 0.01$, respectively.

3. RESULTS AND DISCUSSION

3.1. Synthesis of PDoM. PDoM prepolymers were synthesized through a one-pot polycondensation reaction between MA and diol (Figure 1), adapting to our previous literature.^{26–30} The successful synthesis of PDoM prepolymers is confirmed by the appearance of multiple peaks ~ 4.1 ppm in the ^1H NMR spectra, which are assigned to the protons of the $-\text{CH}_2-$ near the synthesized ester groups (Figure 2A,B). This is further proved by the appearance of the characteristic peak for the ester group $[-\text{C}(=\text{O})\text{OR}]$ at 1737 cm^{-1} in the FTIR spectra of the prepolymers (Figure 2C,D). Along with the increase of the chain length of diol, the ^1H NMR peaks in the high field at 1.3 and 1.6 ppm were heightened (Figure 2A), which can also be reflected from the reinforcement of the characteristic peaks for the methylene group at $2700\text{--}3000\text{ cm}^{-1}$ in the FTIR spectra of the prepolymers (Figure 2C). In the ^1H NMR spectra of POM prepolymers (Figure 2B), along with the ratio of MA: OD increased from 1.0 (pre-POM) to 2.0 (pre-POM-2.0), the height of the peak at 3.3 ppm assigning to the protons of the methylene groups adjacent to the terminal $-\text{OH}$ groups ($-\text{CH}_2-\text{OH}$) decreased, which is further confirmed by the decrease of the characteristic peak in the FTIR spectra of POM prepolymers shown in Figure 2D. The PDoM prepolymers possess abundant reactive carboxyl and hydroxyl groups on their side chains, which can undergo esterification reaction to create cross-linked polymeric networks during the following thermal postpolymerization to give cross-linked PDoM with various cross-linking degrees. The further polymerization or cross-linking of the PDoM polymers is confirmed by the decrease (compared to that of the prepolymers) of the characteristic peak of free carbonyl and hydroxyl groups at $3300\text{--}3700\text{ cm}^{-1}$ in the ATR-FTIR spectra of PDoM polymers shown in Figure 2E,F.

3.2. Characterizations of PDoM. To investigate the effect of cross-linking conditions to the mechanical properties, pre-POM (MA/OD = 1.0:1.0) was chosen as the representative prepolymer for cross-linking condition optimization study. As shown in Figure S2A,B, overall, the increase of cross-linking temperature, elongation of cross-linking time, and application of vacuum all led to higher tensile strengths and Young's moduli, with the effect of the latter two more obviously. However, increasing cross-linking temperature or prolonging cross-linking time also led to the decrease of the elongation at break (Figure S2C), especially when the cross-linking temperature increased from 120 to 130 $^\circ\text{C}$. The fact that the elongation of cross-linking time led to the decrease of the elongation at break can be also proved in the representative stress–strain curves (Figure S2D). Thus, the optimized cross-linking condition of the PDoM polymer was set as 120 $^\circ\text{C}$ for 3 days plus 120 $^\circ\text{C}$ under vacuum for another 3 days. The mechanical properties of the PBM, PHM, POM, PDM, and PDDM, POM-1.2, POM-1.5, and POM-2.0 cross-linked under this condition are shown in Figure 3 and Table S1. It can be seen that the tensile strengths and Young's moduli of PBM,

PHM, POM, PDM, and PDDM were all around or less than 1.0 MPa (Figure 3A,B), indicating the negligible effect of aliphatic diol's chain length to the mechanical strength when the MA/diol ratio = 1.0. This can also be confirmed by the representative stress–strain curves shown in Figure 3D. However, overall, the increase of chain length led to the increase of the elongation at break, with the elongation of PDDM the highest ($243.7 \pm 53.00\%$) (Figure 3C). The POM polymer series were chosen as the representative to investigate the effect of MA/diol ratio to the mechanical strength. As shown in Figure 3A–C, along with the increase of the MA/OD ratio from 1.0 to 2.0, both the mechanical strengths and Young's moduli gradually increased, with the elongations at break being kept in the range of 74–185%. The representative stress–strain curves of POM polymers with different MA/OD ratios shown in Figure 3E also reflect the same trend. POM-2.0 exhibited the highest mechanical strengths, with a tensile strength at 23.8 ± 1.08 MPa and a Young's modulus as high as 72.0 ± 13.09 MPa (Figure 3A,B). The stress–strain curves of all the tested polymer films all exhibit the characteristic behavior of elastomeric materials (Figure 3D,E), and no permanent distortion of the films was found while being subjected to tensile forces during mechanical testing. The favorable elasticity of PDoM make it can quickly recover after being subjected to dynamic loads in a certain extent. Meanwhile, extreme dynamic loads would lead to fatigue failure of the PDoM films. Interestingly, after being immersed in PBS (pH 7.4) for 24 h, the mechanical strengths of the cross-linked PBM, PHM, POM, and PDM films are mostly kept and all increased (Figure S3 and Table S1). This might be caused by the limited residual carboxyl and hydroxyl functionalities in the cross-linked network of PDoM comparing with POC (derived from citric acid and 1,8-octanediol)^{25,26} since MA contains one less carboxyl group than that of citric acid. Few residual functionalities also led to low cross-linking densities and high molecular weight between cross-links comparing that of POC,²⁶ which is confirmed in Table S1. For PDDM, the tensile strength and Young's modulus, especially the latter one, of the swollen film were even significantly enhanced compared to that of the dry film (Table S1). This might be caused by the phase separation in the polymer chains of PDDM during water soak and the formation of physical cross-linking points. The favorable elasticity and the well water resistance of PDoM guarantee their applicability in soft tissue engineering, especially as wound dressing scaffolds.

The thermal properties of the PDoM were characterized by DSC (Figure 3F,G) and TGA (Figure 3H,I). As shown in Figure 3F, along with the aliphatic chain length of diol being increased from 4 to 10, the glass transition temperature (T_g) of the cross-linked polymer films gradually decreased from -10.71 to -31.95 $^\circ\text{C}$. Meanwhile, for PDDM with an aliphatic chain length of 12, there is a melting peak ~ 16 $^\circ\text{C}$ that shows up in the DSC curve (Figure S1). For the POM polymer series, an increase of MA/OD ratios from 1.0 to 2.0 led to the increase of T_g s from -31.77 to 6.41 $^\circ\text{C}$ (Figure 3G), well agreeing with the mechanical testing results that higher MA/OD ratios brought higher mechanical strengths but the elasticity of the polymer reduced overall (Figure 3A–C). All the cross-linked PDoM polymers exhibited considerable stability reflecting by their TGA curves shown in Figure 3H,I, the decomposition temperatures (T_d s) are all >242 $^\circ\text{C}$ except for PHM which possesses a $T_d = 188$ $^\circ\text{C}$. Along with the increase of the MA/OD ratio from 1.0 to 2.0, the T_d s

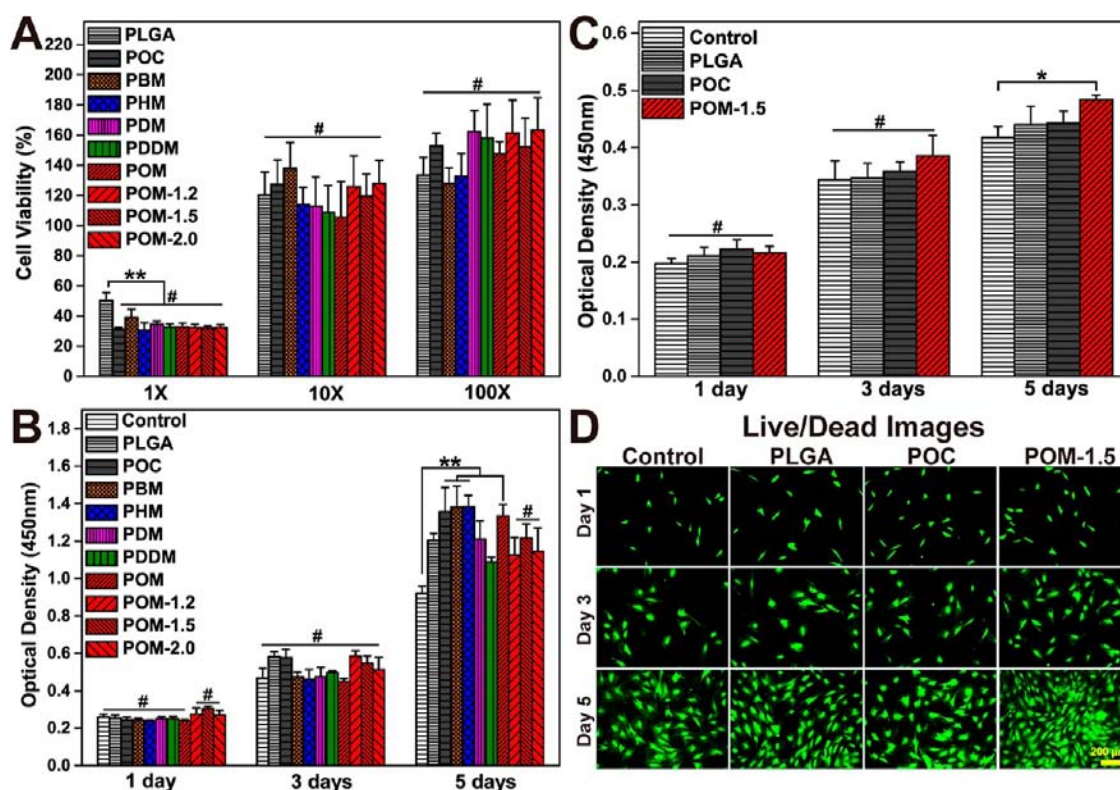


Figure 4. In vitro cytocompatibility of PDoM: (A) cytotoxicity against L929 after 24 h for degradation products of PDoM films and (B) cell proliferation profiles of the 10X degradation products of PDoM films for 1, 3, and 5 days; (C) cell proliferation profiles of rBMSCs after being treated with the 10X degradation products of representative PDoM films for 1, 3, and 5 days and (D) the corresponding Live/Dead staining images. * $p < 0.05$, ** $p < 0.01$, # $p > 0.05$.

gradually decreased from 302 to 242 °C. All the above thermal properties once again confirmed that all the tested PDoM polymers are in the rubbery state at room temperature (T_g s all < 25 °C) and thus possess favorable elasticity. PDDM possesses a melting temperature, which might be one reason that at the wet state, the mechanical strength of which was even enhanced compared with the polymer at the dry state (Table S1).

The wettability of PDoM polymers were assessed by contact angle tests against both water and diiodomethane (CH_2I_2), and the results are shown in Table S2 and Figure S4. All the water-in-air contact angles of the cross-linked PDoM films are in the range of 65–88° (Table S2), suggesting moderate wettability for all PDoM polymers. Prolonging water contact time led to a gradual decrease of contact angle, and the water-in-air contact angles for POM, POM-1.2, and POM-1.5 all decreased from 70 to 88° in the beginning to 30–40° after 30 min; but for POM-2.0, the contact angle decreased from the initial ~85 to ~60° at 20 min and stabilized in the range of 60–65° during 20–30 min (Figure S4). The above results might be caused by that higher MA/OD ratios leads to more hydrophilic carboxyl and hydroxyl groups which can be wetted by water thus reduce the contact angle along with the prolongation of water contact time. Combining with the measured contact angles of the PDoM films to CH_2I_2 , the surface energies (γ_s), as well as their dispersive (γ_s^d) and polar (γ_s^p) components and the ratios of γ_s^p/γ_s (χ^p), were calculated and presented in Table S2. The surface energies of all the tested polymer films were in a small range of 32–45 mJ m^{-2} , once again confirming the moderate wettability of the polymer films.

3.3. Degradation Profiles of PDoM. The degradation profiles of PDoM were investigated by conducting in vitro degradation study in both PBS (pH 7.4) and 0.1 M NaOH solution (for fast degradation) and in vivo degradation study using subcutaneous implantation model on SD rats. As shown in Figure S5A,B, except for PDM and PDDM, all PDoM films completely degraded in 14 h in 0.1 M NaOH solution, both shorter aliphatic chain of diol used and higher MA/OD ratio (for the POM series) led to faster degradation. The PBS degradation study results shown in Figure S5C further confirmed the fact that the shorter aliphatic chain of diol used in PDoM led to faster degradation, with PDDM degraded the slowest. The overall trend reflected by the PBS degradation results for POM series (Figure S5D) agrees well with the degradation results in 0.1 M NaOH (Figure S5B), but the degradation of POM-1.5 was slightly faster than POM-2.0 in PBS. The complete degradation times for POM, POM-1.2, POM-1.5, and POM-2.0 in PBS (pH 7.4) were determined to be 35, 32, 20, and 22 weeks, respectively (Figure S5D). The in vivo degradation results shown in Figure S6 indicate that PBM degraded the fastest in all tested polymer films and completely degraded in 4 weeks, which aligns with the in vitro degradation results (Figure S5A,C). After subcutaneous implantation of polymer films in the backs of SD rats for 12 weeks, the mass losses of POM, PDDM, POM-1.5, POM-2.0, and PLGA were 35.82, 16.27, 56.74, 46.69, and 14.04%, respectively (Figure S6). These results confirm the fast degradability of PDoM comparable with PLGA, well supporting their potential biomedical applications as wound dressing scaffolds.

3.4. Cytocompatibility Evaluation of PDoM. The cytocompatibility of PDoM was estimated by studying the

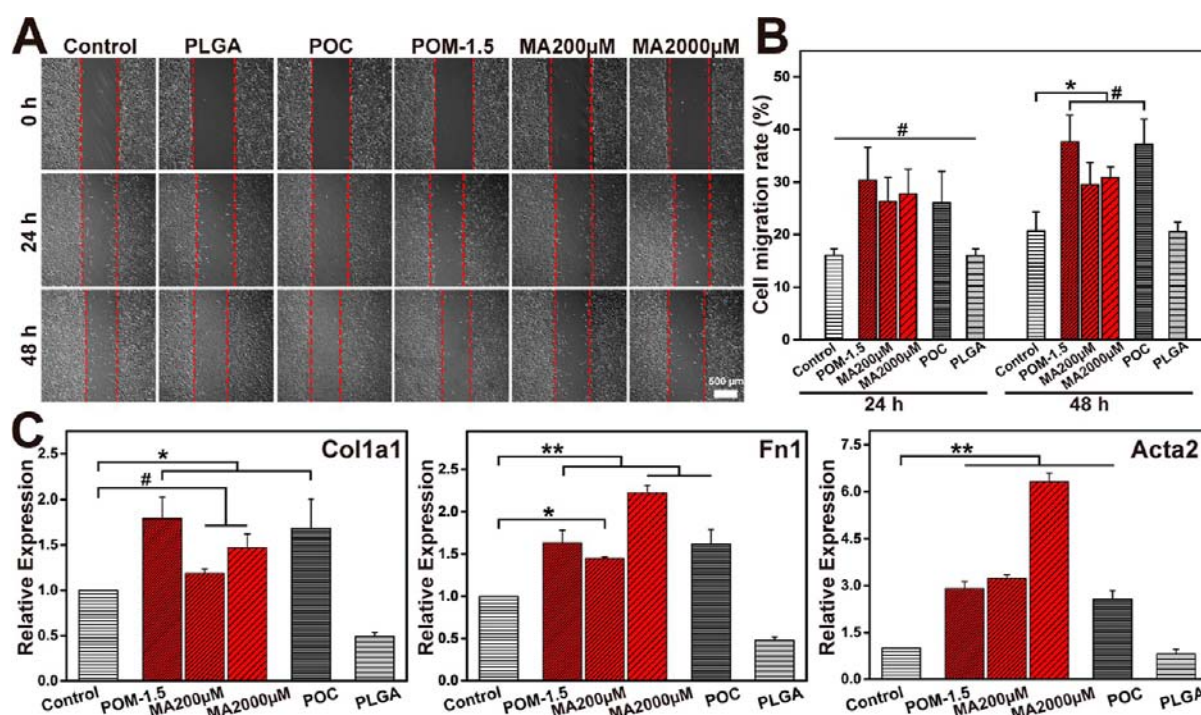


Figure 5. PDm promote fibroblasts' migration, enhance cells' biosynthesis in vitro: (A) images of the scratch test of L929 cultured with MA monomer and 10× diluted degradation products of POM-1.5, PLGA, and POC for 0, 24, and 48 h, and (B) the calculated cell migration rate of different groups; (C) RT-qPCR results of the gene expressions of Col1a1, Fn1, and Acta2 after L929 cells being treated for 24 h by the 10× diluted degradation products of POM-1.5, PLGA, POC, or L-malate solutions. * $p < 0.05$, ** $p < 0.01$, # $p > 0.05$.

cytotoxicity of the degradation products of PDm polymers against both L929 and rBMSCs using the CCK-8 and Live/Dead assays, with PLGA and POC as controls. As shown in Figure 4A, although the 1× degradation products of all tested PDm films showed similar much lower cell viabilities (~30%) compared to PLGA (~50%), the cell viabilities of the 10× and 100× diluted solutions of degradation products of PDm became much higher and were comparable to that of PLGA. The 10× degradation products of PDm were further used to coculture L929 (Figure 4B) and rBMSCs (Figure 4C) for 1, 3, and 5 days. It can be seen that the 10× degradation products of PDm showed favorable cell cytocompatibility and similar cell proliferation profiles as that of POC and PLGA. As a representative PDm polymer, a noticeable cell growth-enhancing effect of POM-1.5 can be seen from the result that the optical density of the POM-1.5 group on day 5 was significantly higher than that of the blank control group (Figure 4C), which can also be reflected in the representative Live/Dead staining images (Figure 4D). The Live/Dead images of POM-1.5 exhibited stretched/elongated cell morphology, once more indicating that POM-1.5 could promote cell attachment and proliferation. These results preliminarily prove the favorable cytocompatibility and proliferation-enhancing properties of the PDm polymers.

The cell cytocompatibility of L-malate monomer (0–5000 µM L-malate, pH 7.4) was also assessed by conducting a CCK-8 assay against rBMSCs. As shown in Figure S7, in a very broad range from 200 to 5000 µM, L-malate induced no cytotoxicity against rBMSCs and can even enhance the proliferation of rBMSCs to a certain extent. The optimal feeding concentrations for exogenous L-malate supplementation were determined to be 200 and 2000 µM, which were subsequently used in a future study.

3.5. PDm Promotes Cell Migration and Gene Expression of Fibroblasts.

Fibroblasts' motility is essential in the healing of skin injuries, and several extracellular matrix proteins, growth factors and cytokines, such as Col1a1, Fn1, and Acta2, are also recognized playing important roles in wound healing.^{32–34} To assess the effect of PDms and MA monomers on the migration of cells, both scratch and transwell assays were conducted using L929 as the cell model with PLGA and POC as controls. As it can be seen from Figure 5A,B, the cell migration rates of POM-1.5 at 24 h was ~30%, much higher than that of the control and PLGA groups (all < 20%), but close to and slightly higher than that of the POC group (~28%). The cell migration rates of 200 and 2000 µM MA at 24 h were also ~28%. Prolongation of treating time to 48 h led to much increase of migration rates to ~38 and ~32% for POM-1.5 and MA solution samples, respectively, and the POM-1.5 group showed significantly higher values than that of the control and PLGA groups (~23%) and comparable to that of the POC (~38%). Similar trends were observed in the transwell assay results (Figure S8). These results indicate that both the degradation products of malate-based polyesters and MA monomer could promote the migration of fibroblasts and thus have a constructive impact on wound healing.

The synthesis of the extracellular matrix (ECM), which can provide a transport system for nutrients and waste products, serves a pivotal function in wound healing.³⁵ Col1a1 and Fn1 are major components of the skin extracellular matrix,³⁶ and Acta2/ α -Sma plays a vital role in wound healing by regulating ECM secretion;³⁷ thus, the expression levels of Col1a1, Fn1, and Acta2 genes by L929 cells after being treated by the 10× diluted degradation product of POM-1.5 or MA solutions for 24 h were investigated by RT-qPCR. As shown in Figure 5C, the expression levels of Col1a1, Fn1, and Acta2 genes of the

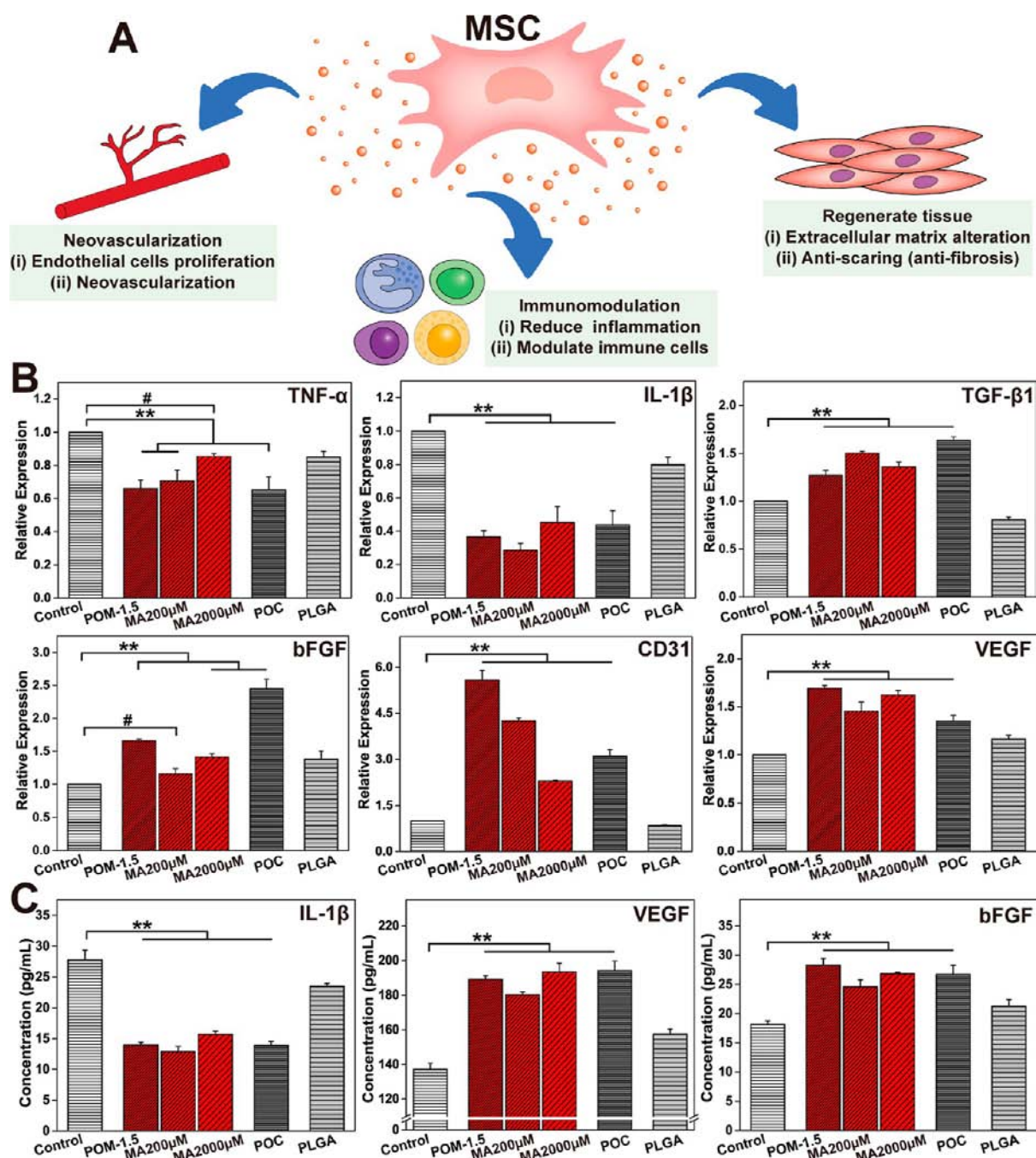


Figure 6. PDoM enhance rBMSCs paracrine level in vitro: (A) representative paracrine effects of stem cells; (B) RT-qPCR results of the gene expressions of TNF- α , IL-1 β , TGF- β 1, CD31, VEGF, and bFGF by rBMSCs; (C) ELISA quantification results of IL-1 β , VEGF, and bFGF secreted from rBMSCs, after rBMSCs being treated by the 10 \times diluted degradation products of POM-1.5, PLGA, POC, or L-malate solutions for 24 h. ** p < 0.01, # p > 0.05.

POM-1.5 sample were determined to be \sim 1.79, \sim 1.64, and \sim 2.90 folds of that of the control group (1.0), all close to that of the POC group which was reported can promote the expression of Col1a1 by osteogenic differentiated MSCs.¹³ The MA solutions also induced enhanced gene expression, especially at 2000 μ M and for Fn1 and Acta2, the Acta2 expression level of the MA2000 μ M sample even reached > 6.31-fold of that of control (Figure 5C). Meanwhile, for PLGA, the expression levels of the tested three genes were all lower than that of the control group (Figure 5C). These results indicate that the expression of wound-healing genes in L929 cells was significantly enhanced by malate-based polyesters,

which might be derived from the related/degraded L-malate from the polymers, suggesting their favorable therapeutic value in facilitating wound healing.

3.6. PDoM Enhances rBMSCs' Paracrine Function.

Bone marrow mesenchymal stem cells (BMSCs) are a type of self-renewing and expandable stem cell with multidirectional differentiative potential and paracrine function and thus were widely used in different wound treatment.^{38–40} The paracrine functions of BMSCs are responsible for improving wound healing, including promoting epidermal cell growth, angiogenesis, collagen deposition, suppressing inflammatory response, and closing wounds (Figure 6A).³⁸ Therefore, the

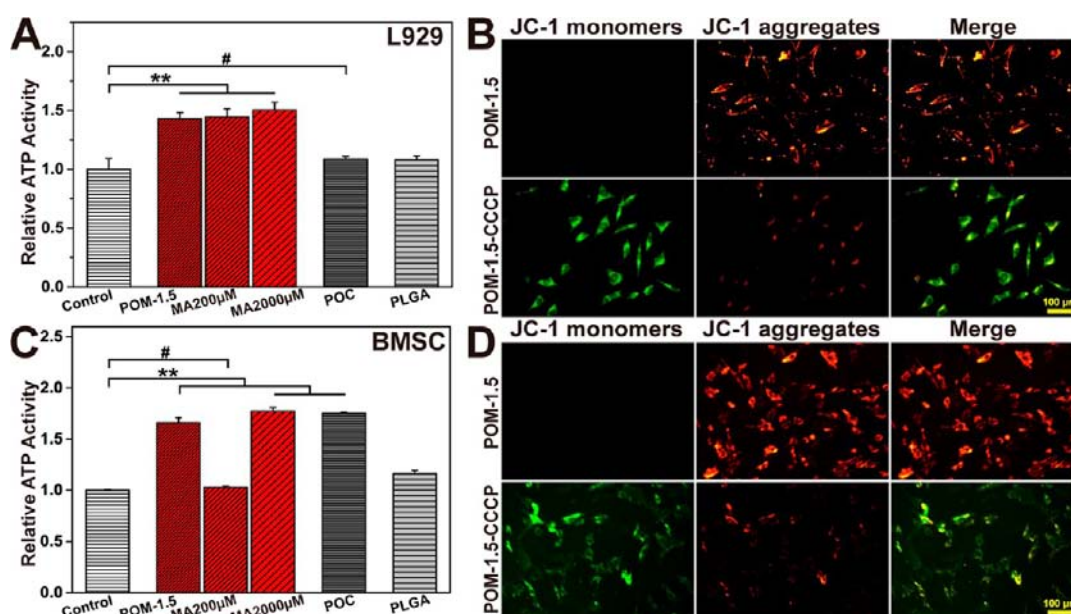


Figure 7. PDoM enhances the cell energy metabolism level in vitro: relative intracellular ATP activities after L929 (A) and rBMSCs (C) being treated with 10 \times diluted degradation products of POM-1.5, POC, PLGA, or MA solutions (200 or 2000 μ M) for 24 h; and the corresponding JC-1 stained images of L929 (B) and rBMSCs (D) cocultured with 10 \times diluted degradation product of POM-1.5 with or without carbonyl cyanide 3-chlorophenylhydrazone (CCCP). ** $p < 0.01$, # $p > 0.05$.

paracrine levels of several relevant factors were measured, namely, TNF- α , IL-1 β , CD31, VEGF, TGF- β 1, and bFGF.

First, the gene expression levels of TNF- α , IL-1 β , TGF- β 1, CD31, VEGF, and bFGF by rBMSCs after being treated with MA solutions and the 10 \times diluted degradation products of PDoM (using POM-1.5 as the representative) for 24 h were studied by RT-qPCR. As shown in Figure 6B, the messenger ribonucleic acid (mRNA) expression levels of pro-inflammatory cytokines, including TNF- α and IL-1 β , in the POM-1.5 and MA groups (except for MA2000 μ M for TNF- α) were all significantly lower than that of the control and PLGA groups and comparable with that of POC group, indicating the favorable anti-inflammatory potential of PDoM. Meanwhile, for TGF- β 1, bFGF, CD31, and VEGF, both POM-1.5 and MA solutions in 200 and 2000 μ M induced significantly enhanced expression comparing with that of the control and PLGA groups, the levels were comparable or even higher than that of POC, implying the favorable activity of PDoM in promoting re-epithelialization and angiogenesis.

Second, the IL-1 β , bFGF, and VEGF levels in the cell culture supernatants of rBMSCs after being treated by MA monomers and 10 \times diluted degradation product of POM-1.5 were determined with the ELISA kit (Figure 6C). The levels of IL-1 β in the POM-1.5 and MA monomers groups were all significantly lower ($p < 0.01$) than that of the control and PLGA groups, and comparable with that of the POC group, further confirming the anti-inflammatory property of PDoM. The levels of bFGF and VEGF in the POM-1.5 and MA monomer groups were all significantly elevated ($p < 0.01$) compared to the control and PLGA groups, and also comparable with that of POC groups, once more confirming the epithelialization and angiogenesis promoting ability. All the above results prove the microenvironment amelioration ability of malate-based polymers by regulating the paracrine of BMSCs, therefore potentially promoting rapid wound healing.

3.7. Energy Metabolism Promotion of PDoM by Participating in the TCA Cycle. To further investigate the

inherent mechanisms of the promotion effect of PDoM to cells' proliferation, migration, biosynthesis, and paracrine, the effect of MA monomer (200 and 2000 μ M) and the degradation products of PDoM (using POM-1.5 as the representative) on the bioenergetic metabolism of both L929 and rBMSCs were studied, with PLGA and POC as controls and cells treated by pure cell growth medium as the blank control. The intracellular ATP levels of different groups measured by the ATP assay kit for rBMSCs and L929 (Figure 7A,C) respectively, all show that the intracellular ATP levels of the POM-1.5 and MA monomer (especially 2000 μ M MA) groups were all significantly higher ($p < 0.01$ except for the MA200 μ M group for rBMSCs) than that of the blank control and PLGA groups. Although the ATP production levels in rBMSCs for the POM-1.5 and POC groups were nearly the same, the intracellular ATP level in L929 of the POM-1.5 group was significantly higher than that of the POC group, implying that L-malate might be a better energy metabolism regulator suitable for broader cell types with different energy-producing modes since it can effectively interlink oxidative phosphorylation (TCA cycle) and glycolysis (two most important energy-producing metabolic pathways in nearly all life forms) via malate-aspartate shuttle.²²

Moreover, the assessment of $\Delta\psi_m$, a crucial factor driving ATP generation in cells, was also carried out using JC-1 as a cationic indicator. Changes in membrane potential over time could be accomplished by JC-1, which aggregates in the matrix to create J-aggregates resulting in high $\Delta\psi_m$ -emitting red fluorescence; conversely, JC-1 cannot aggregate in the mitochondrial matrix to create monomers with low $\Delta\psi_m$ -emitting green fluorescence. After being incubated for 24 h, rBMSC and L929 in the POM-1.5 group all showed a clearly aggregated red fluorescence, confirming higher $\Delta\psi_m$ intensities (Figure 7B,D). However, the red fluorescence was significantly lowered in the POM-1.5-CCCP group due to the effect of the uncoupler carbonyl cyanide 3-chlorophenylhydrazone (CCCP), a respiratory chain inhibitor capable of

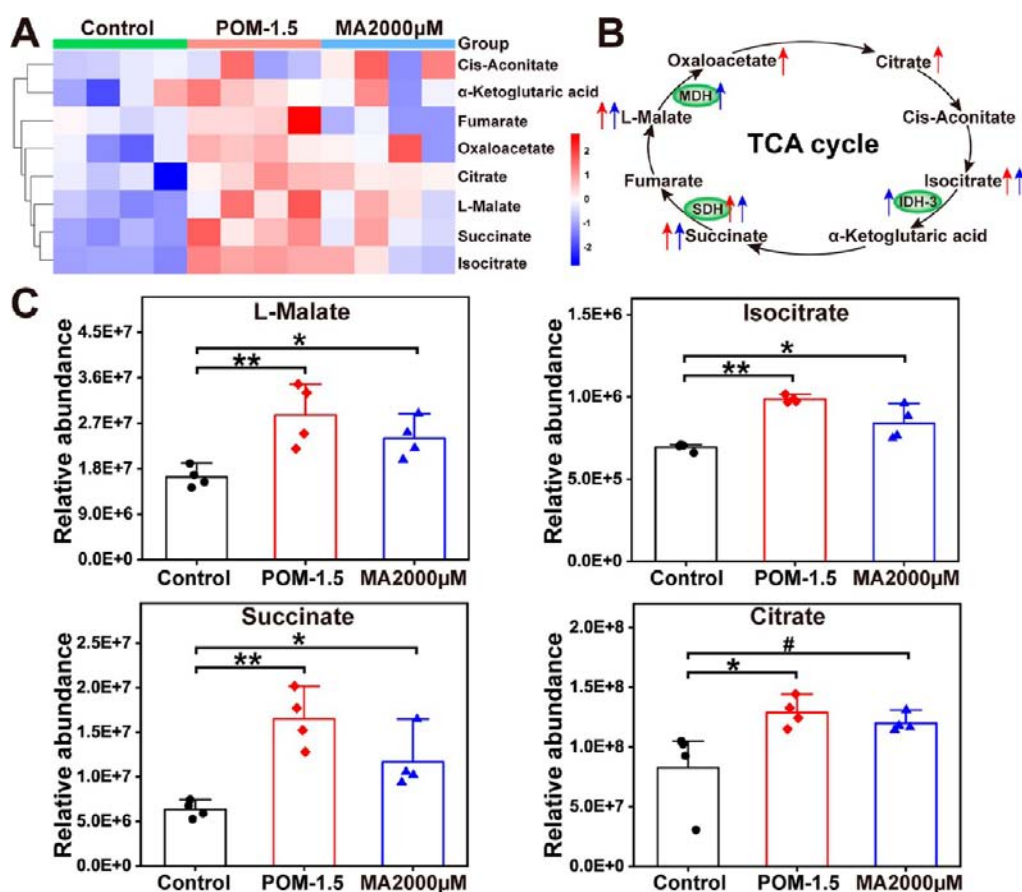


Figure 8. PDm enhances the cell energy metabolism level in vitro by boosting the TCA cycle: (A) relative difference heatmap of the clustered metabolites in rBMSCs after being treated with 10× diluted degradation product of POM-1.5 or MA solution (2000 μM) for 24 h; (B) visualization scheme of the change trend of the TCA cycle metabolites in the POM-1.5 (red) and MA2000 μM (blue) groups comparing the control group [the upward arrow indicates a significant increase ($p < 0.05$) and the downward arrow indicates a significant decrease ($p < 0.05$)]; (C) quantitative relative abundance of L-malate, isocitrate, succinate, and citrate metabolites of the TCA cycle in rBMSCs for POM-1.5, MA2000 μM, and the control groups. The data represent as mean \pm SD ($n = 4$). * $p < 0.05$, ** $p < 0.01$, # $p > 0.05$.

reducing $\Delta\psi_m$ and weakening the ATP synthase's driving force. Collectively, the cellular metabolism results indicated that the degradation products of malate-based polyesters and MA monomer could elevate $\Delta\psi_m$ and promote ATP production by both L929 and rBMSCs, implying that malate-based polymers could provide additional energy resources for tissue regeneration. To assess the link between malate-based polyesters and TCA cycle, RT-qPCR was utilized to determine the expression levels of genes related to the critical rate-limiting enzymes of the TCA cycle, including IDH-3, SDH, and MDH. The mRNA abundances of the transcription genes of IDH-3, SDH, and MDH, of the POM-1.5 and MA solution (especially MA2000 μM) group were significantly ($p < 0.01$) higher than that of the PLGA and blank control groups (Figure S9A). Particularly, the level of MDH showed the most significant increase ($p < 0.01$) in the MA2000 μM group, indicating that PDm or other malate-based polymers are able to boost the TCA cycle by promoting mitochondrial biogenesis.

To further and directly verify the effect of malate to the TCA cycle by entering mitochondria, rBMSCs were treated by both 10× diluted degradation product of POM-1.5 and MA2000 μM for 24 h, and the contents of intracellular metabolites related to TCA cycle were measured using liquid chromatography–mass spectrometry (LC–MS). A hierarchical cluster analysis (HCA) heatmap was utilized to visualize the intensity

of each metabolite, highlighting eight significant metabolites in the TCA cycle (Figure 8A). The abundances of the key metabolites in the TCA cycle, such as L-malate, isocitrate, succinate, and citrate, for the POM-1.5 and MA2000 μM groups were significantly ($p < 0.05$ except for the MA2000 μM group for citrate) higher than that of the control groups (Figure 8B,C). For some metabolites such as oxaloacetate, cis-aconitate, α -ketoglutaric acid, and fumarate, their abundance in the POM-1.5 and MA2000 μM groups were also higher than the control group but had no significant difference ($p > 0.05$ except for the POM-1.5 group for oxaloacetate) (Figure S9B). Given the limited parallel specimens and possible data errors, the above results still can confirm that increase of exogenous malate level also promotes the increase of the contents of other key metabolites in the TCA cycle.

To sum up, these results provide conclusive evidence proving that the increase of cellular malate concentration via the uptake of the degradation products of malate-based polyester by cells could promote energy metabolism including elevate ATP production and increase the abundance of critical metabolites by participating in the TCA cycle.

3.8. Foreign Body Response Evaluations. The in vivo cytocompatibility of cross-linked PDm films was studied by subcutaneously implanting PBM, POM, PDDM, and POM-1.5 films in SD rats, respectively, using PLGA as control. As shown in Figure S10, all samples exhibited a mild acute inflammatory

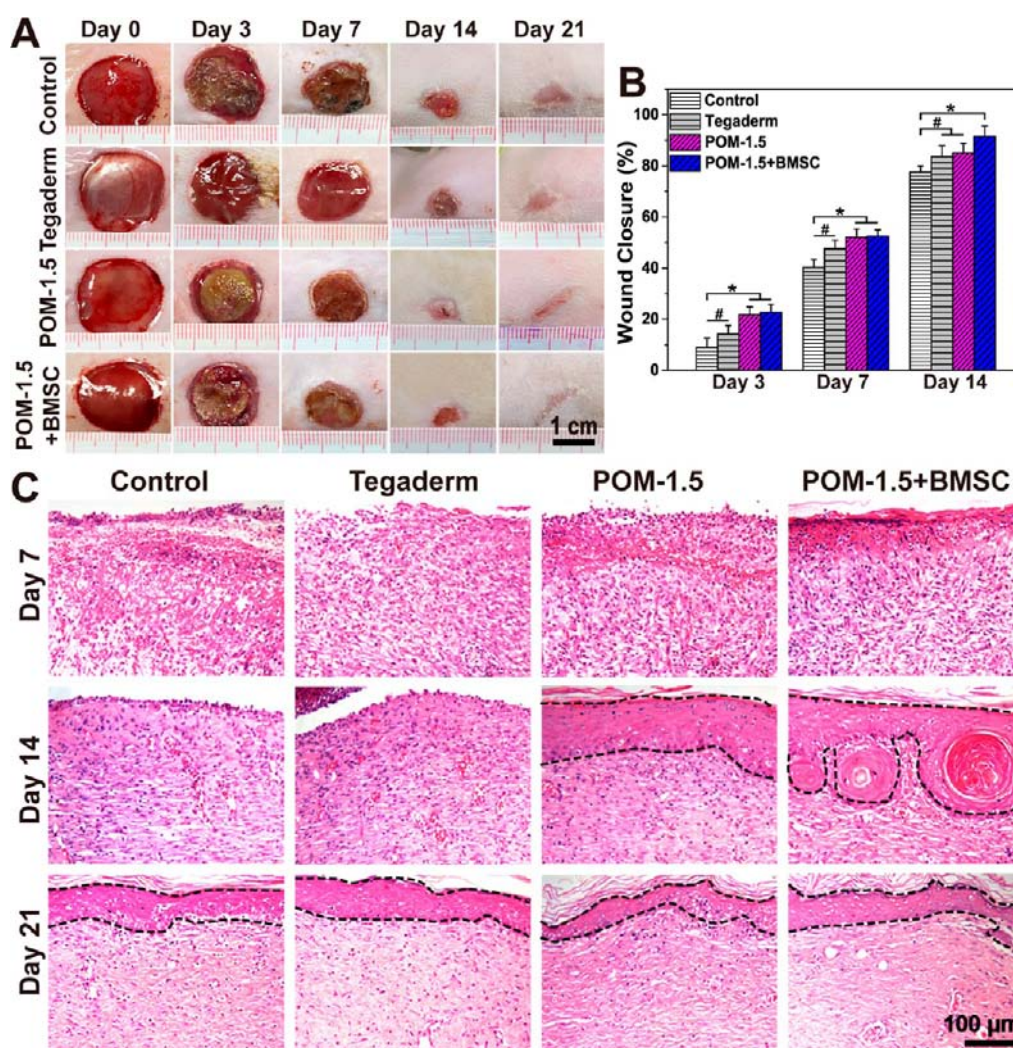


Figure 9. Wound healing evaluations in vivo: (A) representative photographs reflecting the wound healing process for control, Tegaderm, POM-1.5, and POM-1.5+BMSC groups on 0, 3rd, 7th, 14th, and 21st day; (B) the wound closure rates for various groups during 14 days; and (C) representative H & E staining images for wound healing after treatment of various groups during 21 days, scale bar: 100 μm (black dotted lines indicate the epithelium border). * $p < 0.05$, # $p > 0.05$.

response after 1 week of implantation, confirming by cell infiltration (H & E staining, Figure S10A) and the presence of CD11b-positive cells in tissues adjacent to the implanted polymer films (CD11b staining, Figure S10B). This is an expected normal process, consistent with the entry of most foreign bodies into the body; and the inflammatory response of all tested PDoM polymers was similar to that of PLGA, reflecting from the comparable total cell numbers and cell amounts of CD11b-positive cells of different groups (Figure S10C,D). Meanwhile, the cell densities around different polymer implants decreased over time, with no significant statistical differences between different groups at weeks 4 and 12 (Figure S10C). After 12 weeks of implantation, very few CD11b-positive cells could be observed, indicating the decay of an acute inflammatory response (Figure S10D). These results further prove the biocompatibility of PDoM polymers in vivo, preliminarily confirming the feasibility of PDoM polymers in the following in vivo wound healing applications.

3.9. PDoM Scaffolds Support Cell Attachment and Proliferation. Tissue engineering porous scaffolds could provide a favorable microenvironment similar to natural ECM for cell growth and proliferation.^{41,42} As a representative

of PDoM, elastic POM-1.5 was fabricated into porous soft scaffold and rBMSCs were also seeded on the scaffold and cultured for 5 days; the photograph and SEM images of the scaffold and cell-laden scaffold are shown in Figure S11. The POM-1.5 scaffold looks as a yellow-colored disk with obvious pores (Figure S11A1), and the pores were cube-shaped with a size ranging 125–200 μm , which are created by salt crystals as the porogen (Figure S11A2). From Figure S11A3,A4, it can be seen that rBMSCs were well attached and spread on the surface and in the pores of the scaffold, indicating that the POM-1.5 scaffold could support the adhesion and proliferation of rBMSCs.

3.10. In Vivo Wound Healing Evaluation. A full-thickness rat skin defect repair test was conducted to validate the efficacy of PDoM scaffolds combined with BMSCs in vivo as a wound dressing and assess its potential applications in wound healing. The POM-1.5 scaffold was selected as a representative of PDoM polymer scaffolds, and alive rBMSCs were also laden on POM-1.5 scaffold to create a POM-1.5 + BMSC sample, commercially available Tegaderm dressing, and the wound left untreated were used as controls. After surgery, the wound areas all shrank over time for the four groups

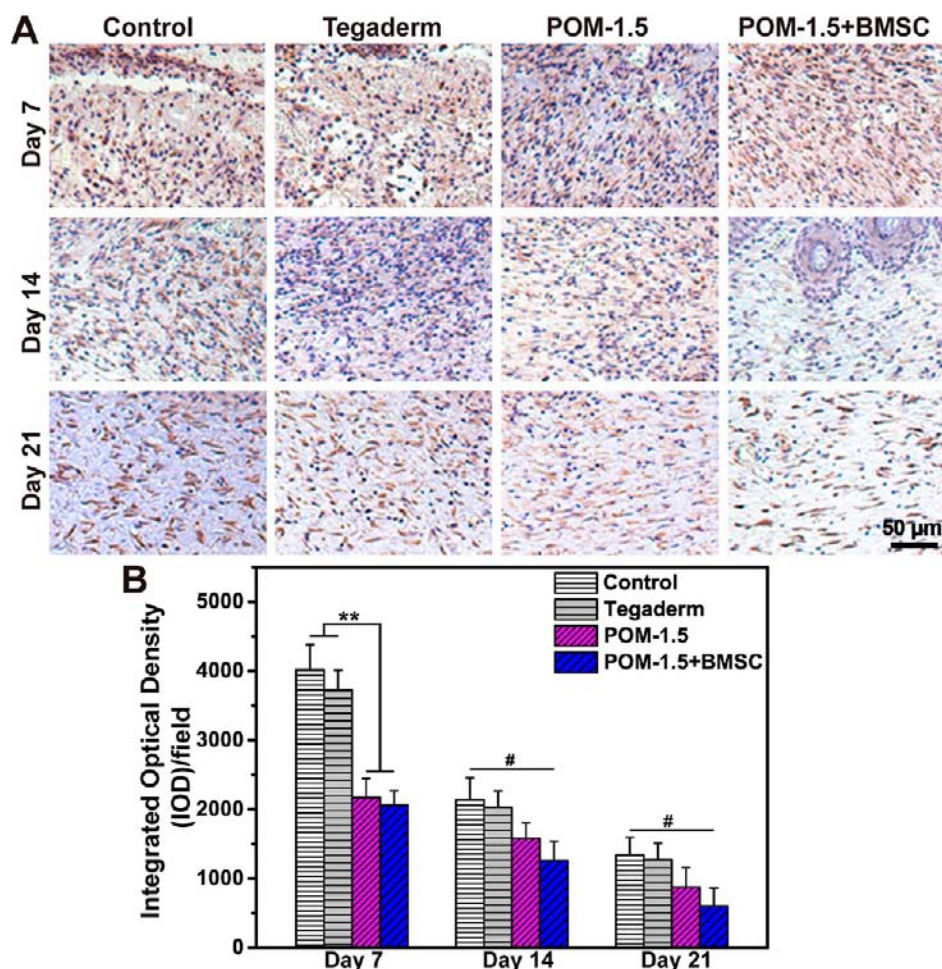


Figure 10. Effect of PDoM scaffolds on immunomodulation: (A) IL-1 β immunohistochemical stained images of wound tissues on the 7th, 14th, and 21st day after surgery; (B) quantified data of the integrated optical density (IOD) of IL-1 β . ** $p < 0.01$, # $p > 0.05$.

(Figure 9A), but the wound closure rates of the POM-1.5 and POM-1.5 + BMSC groups were significantly higher ($p < 0.05$) than that of the control and Tegaderm groups, especially on days 3 and 7 (Figure 9B). After 14 days' treatment, the wound closure rates were approximately 91.52 and 84.95% for POM-1.5 + BMSC and POM-1.5 groups, respectively, whereas those of the control and Tegaderm groups were 77.64 and 83.64%, respectively (Figure 9B). At the end of the 21 day period, the wounds that were dressed with Tegaderm were partially healed, whereas those treated with POM-1.5 + BMSC had adequately closed and even exhibited hair regeneration in some rats. Taken together, these results indicate that the combination of POM-1.5 scaffold with rBMSCs can considerably accelerate the rate and improve the quality of wound healing.

To further evaluate the process of wound healing, histological examination was performed using H & E and Masson's trichrome staining. The histologic assessment was conducted to evaluate the progression of wound healing in different phases. On day 7, an augmented quantity of inflammatory cells was evident in all the four groups as shown in the H & E staining images (Figure 9C), revealing the onset of an inflammatory response. Inflammatory cell counts reduced over time as healing progressed (between days 7 and 21) while the formation of epithelial tissue gradually took place in all groups. After 14 days' treatment, the POM-1.5 + BMSC

group displayed complete re-epithelialization and almost a normal epidermal structure. In contrast, incomplete formation of skin structure was observed in the Tegaderm and control groups, along with the persistence of inflammatory cells in the dermis structure (Figure 9C).

Collagen, as the main structural protein present in the skin, is crucial for both wound healing and dermal remodeling.⁴³ Masson's trichrome staining images of the healing area until 21 days after surgery are shown in Figure S12. All groups showed a certain degree of collagen deposition at 7 days following initial wound formation. The POM-1.5 scaffold-treated wound exhibited significantly higher ($p < 0.05$) collagen density than the control group after 14 days. As shown in Figure S12A,B, the quantitative image analysis results revealed a significantly higher collagen density in the POM-1.5 + BMSC (~62%) group than the control (~35%), Tegaderm (~43%), and POM-1.5 (~57%) groups after 14 days' healing. After 21 days of healing, parallel collagen fibers and well-aligned granulation tissues were observed in both the POM-1.5 + BMSC and POM-1.5 groups (Figure S12A). A higher collagen content in the scaffold combined with the BMSC group indicates a better healing effect as collagen deposition and granulation formation are positively correlated with wound healing.

Critical molecular and cellular mechanisms are also involved in wound healing. In the initial stages of the wound healing process, the expression of pro-inflammatory factors is crucial

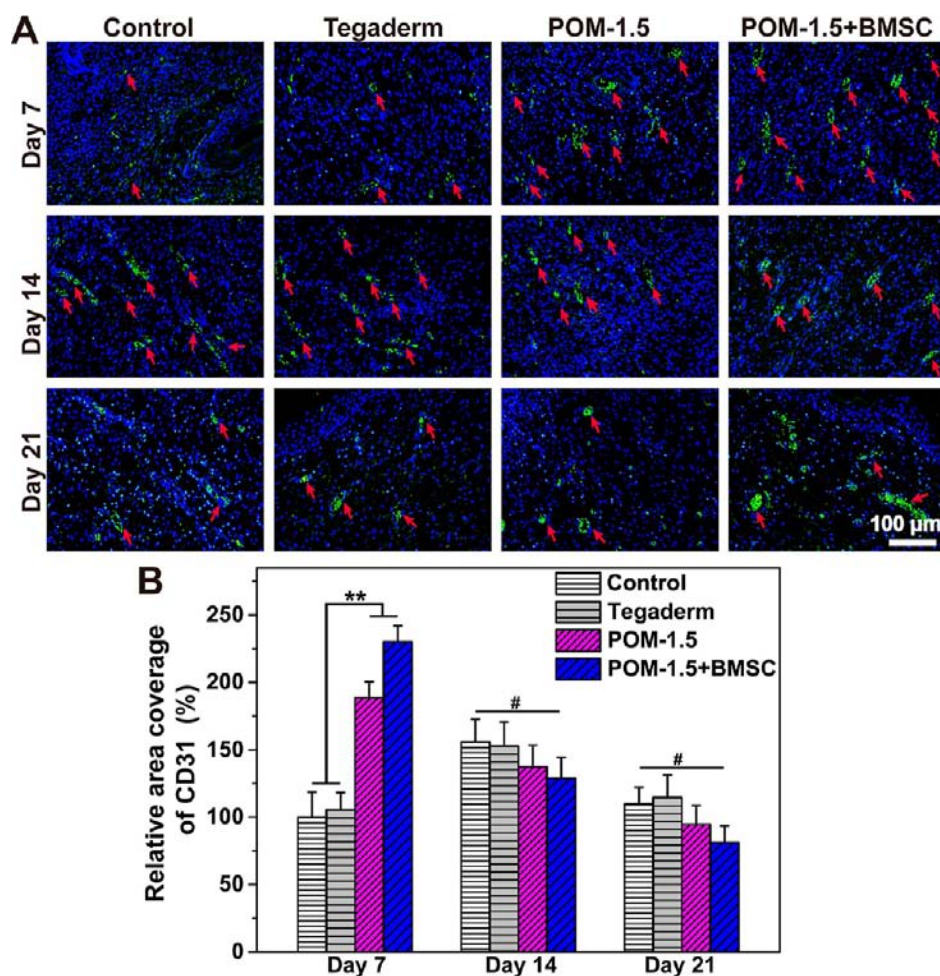


Figure 11. Effect of PDoM scaffolds on neovascularization: (A) CD31 immunofluorescence stained images (red arrows represent new blood vessels) of wound tissues on the 7th, 14th, and 21st day after surgery; (B) the relative fluorescent area percentage of CD31 (D) (the control group on day 7 was set as 100%). ** $p < 0.01$, # $p > 0.05$.

for wound repair.⁴⁴ Nevertheless, an extended inflammatory phase caused by prolonged upregulation of proinflammatory factors can lead to delayed wound healing.⁴⁵ To evaluate the extent of the inflammatory response, the levels of IL-1 β , a representative pro-inflammatory factor, were studied by IL-1 β immunohistochemical staining (Figure 10A). As shown in Figure 10A,B, the numbers of inflammatory cells steadily declined throughout the tissue-healing process. IL-1 β expression was partially inhibited at different time points in the POM-1.5 and POM-1.5 + BMSC groups compared to that in the control and Tegaderm groups, indicating considerable anti-inflammatory ability of POM-1.5 and POM-1.5 + BMSC. Neovascularization plays a vital role in wound healing since it provides the necessary nutrients and oxygen to the tissues along with the removal of waste products and carbon dioxide.⁴⁶ To determine the degree of neovascularization during healing, VEGF immunohistochemical and CD31 immunofluorescence staining was performed (Figures 11A and S13A). According to Figures 11B and S13B, the POM-1.5 and POM-1.5 + BMSC groups exhibited significantly higher expression of both CD31 ($p < 0.01$) and VEGF ($p < 0.05$) when compared to the Tegaderm and control groups on day 7. Meanwhile, on days 14 and 21, the expression levels of both CD31 and VEGF for the POM-1.5 and POM-1.5 + BMSC groups were all lower than those of the other two groups; this

might imply the fast wound healing of the two scaffold groups and thus the need of neovascularization moderated after 7 days. These results indicate that the application of PDoM and stem cells can accelerate wound closure and enhance neovascularization during the initial phases of healing. Thus, it is further revealed that the PDoM scaffold combined with BMSCs could significantly decrease early inflammation and enhance neovascularization as evidenced by a decreased expression of the pro-inflammatory factor IL-1 β and elevated expression of the pro-angiogenic factors CD31 and VEGF (especially in the early wound healing phases), thus promoting the regeneration of the entire skin and improving the healing of dermal wounds.

4. CONCLUSIONS

In summary, through the facile polycondensation reaction between L-malic acid and aliphatic diol to obtain poly(diols L-malate) (PDoM) prepolymers, followed by scaffold fabrication and thermal-induced postpolymerization, a family of biodegradable and biocompatible L-malate-based PDoM bioenergetic scaffold was developed. The degradation products of the developed PDoM scaffolds and L-malate monomer were proven to regulate the metabolic microenvironment by entering the mitochondria and participating in the TCA cycle to elevate intracellular ATP levels and thus promote the

cellular biosynthesis, including the production of Col1a1, Fn1, and Acta2/ α -Sma. The porous and interconnected structure of the PDoM scaffold makes it suitable as a matrix for the 3D BMSC culture and was demonstrated to support the growth of the cocultured rBMSCs and promote their paracrine function, including the secretion of bioactive molecules (such as VEGF, TGF- β 1, and bFGF), and this stem cell-scaffold architecture was proven to improve the wound microenvironment by inducing an increase in key genes involved in the repair process in a critical full-thickness skin defect model on rats. The animal study revealed that the groups treated with POM-1.5 + BMSCs exhibited superior wound healing outcomes compared to the control and Tegaderm groups, with regard to both wound closure and collagen metabolism. Notably, the evaluation of histomorphology and IL-1 β , VEGF, and CD31 expression levels throughout the wound healing process affirmed its improved wound healing efficacy by boosting the expression of angiogenic factors while suppressing inflammatory factors. Thus, we confirm that these malate-based bioenergy boosting scaffold materials possess great application potential in the field of tissue engineering and regenerative medicine and can be universally expanded from skin wound healing to all tissue engineering scenarios where energy metabolism and cell biosynthesis need to be enhanced to realize fast healing and the paracrine functions of related cells also need to be regulated to provide a more suitable tissue healing microenvironment. However, in the future, polymer design needs to be further improved to introduce more energetic substances, such as organic phosphate-containing chemicals or metallic ions affecting energy metabolism, and to regulate the mechanical property and the release rates of energetic substances; the activation of energy metabolism and redox homeostasis also need to be balanced to eliminate possible oxidative stress.

■ ASSOCIATED CONTENT

SI Supporting Information

The Supporting Information is available free of charge at <https://pubs.acs.org/doi/10.1021/acsami.3c09394>.

Mechanical properties of dry and swollen cross-linked PDoM films, cross-linking densities, and the molecular weight between cross-links of the films; contact angles of PDoM polymers to water and CH₂I₂ and the calculated surface energies and their components; primer sequences; DSC curve of PDDM; mechanical properties of POM polymers with different cross-linking conditions; wet mechanical properties; the water-in-air contact angle (θ) versus time curves of cross-linked POM with different MA/OD ratios; degradation study of PDoM in vitro, in 0.1 M NaOH and PBS (pH 7.4) solution; in vivo degradation profiles of PDoM polymers and PLGA for 1, 4, and 12 weeks; cell viabilities of rBMSCs after being treatment with L-malate solutions with different concentrations for 24 h; transwell assay results of L929 cultured with MA monomer and polymers fragments for 24 h; PDoM enhancing the cell energy metabolism level in vitro; foreign body response evaluations; photograph and SEM images of PDoM porous scaffold and rBMSC-laden scaffold; effect of PDoM scaffolds on collagen deposition; and effect of PDoM scaffolds on neovascularization (PDF)

■ AUTHOR INFORMATION

Corresponding Author

Jinshan Guo – Department of Histology and Embryology, GDMPA Key Laboratory of Key Technologies for Cosmetics Safety and Efficacy Evaluation, NMPA Key Laboratory for Safety Evaluation of Cosmetics, School of Basic Medical Sciences, Southern Medical University, Guangzhou 510515, P. R. China; orcid.org/0000-0001-8097-4902; Email: jsguo4127@smu.edu.cn, jsguo4127@163.com

Authors

Min Wu – Department of Histology and Embryology, GDMPA Key Laboratory of Key Technologies for Cosmetics Safety and Efficacy Evaluation, NMPA Key Laboratory for Safety Evaluation of Cosmetics, School of Basic Medical Sciences, Southern Medical University, Guangzhou 510515, P. R. China

Yitao Zhao – Department of Histology and Embryology, GDMPA Key Laboratory of Key Technologies for Cosmetics Safety and Efficacy Evaluation, NMPA Key Laboratory for Safety Evaluation of Cosmetics, School of Basic Medical Sciences, Southern Medical University, Guangzhou 510515, P. R. China

Meihan Tao – Department of Histology and Embryology, GDMPA Key Laboratory of Key Technologies for Cosmetics Safety and Efficacy Evaluation, NMPA Key Laboratory for Safety Evaluation of Cosmetics, School of Basic Medical Sciences, Southern Medical University, Guangzhou 510515, P. R. China

Meimei Fu – Department of Histology and Embryology, GDMPA Key Laboratory of Key Technologies for Cosmetics Safety and Efficacy Evaluation, NMPA Key Laboratory for Safety Evaluation of Cosmetics, School of Basic Medical Sciences, Southern Medical University, Guangzhou 510515, P. R. China

Yue Wang – Department of Histology and Embryology, GDMPA Key Laboratory of Key Technologies for Cosmetics Safety and Efficacy Evaluation, NMPA Key Laboratory for Safety Evaluation of Cosmetics, School of Basic Medical Sciences, Southern Medical University, Guangzhou 510515, P. R. China

Qi Liu – Regenerative Medicine and Tissue Repair Research Center, Huangpu Institute of Materials, Guangzhou 511363, P. R. China

Zhihui Lu – Department of Histology and Embryology, GDMPA Key Laboratory of Key Technologies for Cosmetics Safety and Efficacy Evaluation, NMPA Key Laboratory for Safety Evaluation of Cosmetics, School of Basic Medical Sciences, Southern Medical University, Guangzhou 510515, P. R. China; Regenerative Medicine and Tissue Repair Research Center, Huangpu Institute of Materials, Guangzhou 511363, P. R. China

Complete contact information is available at: <https://pubs.acs.org/doi/10.1021/acsami.3c09394>

Author Contributions

[§]M.W. and Y.Z. contributed equally to this work.

Notes

The authors declare no competing financial interest.

ACKNOWLEDGMENTS

This work was supported by the Natural Science Foundation of China (grant nos. 82272453, U21A2099, and 82102545), the Youth Talent of Guangdong Special Support Program (0620220207), the China Postdoctoral Science Foundation (grant no. 2022M721515), the Basic and Applied Basic Research Project of Guangzhou City (202201011774), and the Open Program from Guangdong Provincial Key Laboratory of Bone and Joint Degeneration Disease.

REFERENCES

- (1) Safina, I.; Embree, M. C. Biomaterials for Recruiting and Activating Endogenous Stem Cells in Situ Tissue Regeneration. *Acta Biomater.* **2022**, *143*, 26–38.
- (2) Stack, M. E.; Mishra, S.; Parimala Chelvi Ratnamani, M.; Wang, H.; Gold, L. I.; Wang, H. Biomimetic Extracellular Matrix Nanofibers Electrospun with Calreticulin Promote Synergistic Activity for Tissue Regeneration. *ACS Appl. Mater. Interfaces* **2022**, *14*, 51683–51696.
- (3) Costello, L.; Dicolandrea, T.; Tasseff, R.; Isfort, R.; Bascom, C.; von Zglinicki, T.; Przyborski, S. Tissue Engineering Strategies to Bioengineer the Ageing Skin Phenotype in Vitro. *Aging Cell* **2022**, *21*, No. e13550.
- (4) Griffin, D. R.; Archang, M. M.; Kuan, C. H.; Weaver, W. M.; Weinstein, J. S.; Feng, A. C.; Ruccia, A.; Sideris, E.; Ragkousis, V.; Koh, J.; Plikus, M. V.; Di Carlo, D.; Segura, T.; Scumpia, P. O. Activating an Adaptive Immune Response from a Hydrogel Scaffold Imparts Regenerative Wound Healing. *Nat. Mater.* **2021**, *20*, 560–569.
- (5) Loebel, C.; Burdick, J. A. Engineering Stem and Stromal Cell Therapies for Musculoskeletal Tissue Repair. *Cell Stem Cell* **2018**, *22*, 325–339.
- (6) Midgley, A. C.; Wei, Y.; Li, Z.; Kong, D.; Zhao, Q. Nitric-Oxide-Releasing Biomaterial Regulation of the Stem Cell Microenvironment in Regenerative Medicine. *Adv. Mater.* **2020**, *32*, No. e1805818.
- (7) Voog, J.; Jones, D. L. Stem Cells and the Niche: a Dynamic Duo. *Cell Stem Cell* **2010**, *6*, 103–115.
- (8) Lane, S. W.; Williams, D. A.; Watt, F. M. Modulating the Stem Cell Niche for Tissue Regeneration. *Nat. Biotechnol.* **2014**, *32*, 795–803.
- (9) Young, K.; Eudy, E.; Bell, R.; Loberg, M. A.; Stearns, T.; Sharma, D.; Velten, L.; Haas, S.; Filippi, M. D.; Trowbridge, J. J. Decline in IGF1 in the Bone Marrow Microenvironment Initiates Hematopoietic Stem Cell Aging. *Cell Stem Cell* **2021**, *28*, 1473–1482.e7.
- (10) DeBerardinis, R. J.; Mancuso, A.; Daikhin, E.; Nissim, I.; Yudkoff, M.; Wehrli, S.; Thompson, C. B. Beyond Aerobic Glycolysis: Transformed Cells can Engage in Glutamine Metabolism that Exceeds the Requirement for Protein and Nucleotide Synthesis. *Proc. Natl. Acad. Sci. U.S.A.* **2007**, *104*, 19345–19350.
- (11) Gao, P.; Tchernyshyov, I.; Chang, T. C.; Lee, Y. S.; Kita, K.; Ochi, T.; Zeller, K. I.; De Marzo, A. M.; Van Eyk, J. E.; Mendell, J. T.; Dang, C. V. C-Myc Suppression of MiR-23a/b Enhances Mitochondrial Glutaminase Expression and Glutamine Metabolism. *Nature* **2009**, *458*, 762–765.
- (12) Wei, J.; Shimazu, J.; Makinistoglu, M. P.; Maurizi, A.; Kajimura, D.; Zong, H.; Takarada, T.; Iezaki, T.; Pessin, J. E.; Hinoi, E.; Karsenty, G. Glucose Uptake and Runx2 Synergize to Orchestrate Osteoblast Differentiation and Bone Formation. *Cell* **2015**, *161*, 1576–1591.
- (13) Ma, C.; Tian, X.; Kim, J. P.; Xie, D.; Ao, X.; Shan, D.; Lin, Q.; Hudock, M. R.; Bai, X.; Yang, J. Citrate-Based Materials Fuel Human Stem Cells by Metabonegenic Regulation. *Proc. Natl. Acad. Sci. U.S.A.* **2018**, *115*, E11741–E11750.
- (14) Ma, C.; Kuzma, M. L.; Bai, X.; Yang, J. Biomaterial-Based Metabolic Regulation in Regenerative Engineering. *Adv. Sci.* **2019**, *6*, 1900819.
- (15) Zhang, C. S.; Hawley, S. A.; Zong, Y.; Li, M.; Wang, Z.; Gray, A.; Ma, T.; Cui, J.; Feng, J. W.; Zhu, M.; Wu, Y. Q.; Li, T. Y.; Ye, Z.; Lin, S. Y.; Yin, H.; Piao, H. L.; Hardie, D. G.; Lin, S. C. Fructose-1,6-Bisphosphate and Aldolase Mediate Glucose Sensing by AMPK. *Nature* **2017**, *548*, 112–116.
- (16) Voss, K.; Hong, H. S.; Bader, J. E.; Sugiura, A.; Lyssiotis, C. A.; Rathmell, J. C. A Guide to Interrogating Immunometabolism. *Nat. Rev. Immunol.* **2021**, *21*, 637–652.
- (17) Shyh-Chang, N.; Zhu, H.; Yvanka de Soysa, T.; Shinoda, G.; Seligson, M. T.; Tsanov, K. M.; Nguyen, L.; Asara, J. M.; Cantley, L. C.; Daley, G. Q. Lin28 Enhances Tissue Repair by Reprogramming Cellular Metabolism. *Cell* **2013**, *155*, 778–792.
- (18) Dai, Z.; Xia, C.; Zhao, T.; Wang, H.; Tian, H.; Xu, O.; Zhu, X.; Zhang, J.; Chen, P. Platelet-Derived Extracellular Vesicles Ameliorate Intervertebral Disc Degeneration by Alleviating Mitochondrial Dysfunction. *Mater. Today Bio* **2023**, *18*, 100512.
- (19) Zhang, S.; Weinberg, S.; DeBerge, M.; Gainullina, A.; Schipma, M.; Kinchen, J. M.; Ben-Sahra, I.; Gius, D. R.; Yvan-Charvet, L.; Chandel, N. S.; Schumacker, P. T.; Thorp, E. B. Efferocytosis Fuels Requirements of Fatty Acid Oxidation and the Electron Transport Chain to Polarize Macrophages for Tissue Repair. *Cell Metab.* **2019**, *29*, 443–456.e5.
- (20) Schiffmann, L. M.; Werthenbach, J. P.; Heintges-Kleinhofer, F.; Seeger, J. M.; Fritsch, M.; Günther, S. D.; Willenborg, S.; Brodesser, S.; Lucas, C.; Jüngst, C.; Albert, M. S.; Schorn, F.; Witt, A.; Moraes, C. T.; Bruns, C. J.; Pasparakis, M.; Krönke, M.; Eming, S. A.; Coutelle, O.; Kashkar, H. Mitochondrial Respiration Controls Neoangiogenesis during Wound Healing and Tumour Growth. *Nat. Commun.* **2020**, *11*, 3653.
- (21) Liu, H.; Du, Y.; St-Pierre, J. P.; Bergholt, M. S.; Autefage, H.; Wang, J.; Cai, M.; Yang, G.; Stevens, M. M.; Zhang, S. Bioenergetic-Active Materials Enhance Tissue Regeneration by Modulating Cellular Metabolic State. *Sci. Adv.* **2020**, *6*, No. eaay7608.
- (22) Lee, W. C.; Ji, X.; Nissim, I.; Long, F. Malic Enzyme Couples Mitochondria with Aerobic Glycolysis in Osteoblasts. *Cell Rep.* **2020**, *32*, 108108.
- (23) Wang, Y.; Ameer, G. A.; Sheppard, B. J.; Langer, R. A Tough Biodegradable Elastomer. *Nat. Biotechnol.* **2002**, *20*, 602–606.
- (24) Yang, J.; Bei, J.; Wang, S. Enhanced Cell Affinity of Poly (D,L-lactide) by Combining Plasma Treatment with Collagen Anchorage. *Biomaterials* **2002**, *23*, 2607–2614.
- (25) Yang, J.; Shi, G.; Bei, J.; Wang, S.; Cao, Y.; Shang, Q.; Yang, G.; Wang, W. Fabrication and Surface Modification of Macroporous Poly(L-lactic acid) and Poly(L-lactic-co-glycolic acid) (70/30) Cell Scaffolds for Human Skin Fibroblast Cell Culture. *J. Biomed. Mater. Res.* **2002**, *62*, 438–446.
- (26) Yang, J.; Webb, A. R.; Pickerill, S. J.; Hageman, G.; Ameer, G. A. Synthesis and Evaluation of Poly(diols citrate) Biodegradable Elastomers. *Biomaterials* **2006**, *27*, 1889–1898.
- (27) Guo, J.; Xie, Z.; Tran, R. T.; Xie, D.; Jin, D.; Bai, X.; Yang, J. Click Chemistry Plays a Dual Role in Biodegradable Polymer Design. *Adv. Mater.* **2014**, *26*, 1906–1911.
- (28) Fu, M.; Zhao, Y.; Wang, Y.; Li, Y.; Wu, M.; Liu, Q.; Hou, Z.; Lu, Z.; Wu, K.; Guo, J. On-Demand Removable Self-Healing and pH-Responsive Europium-Releasing Adhesive Dressing Enables Inflammatory Microenvironment Modulation and Angiogenesis for Diabetic Wound Healing. *Small* **2023**, *19*, No. e2205489.
- (29) Wu, K.; Fu, M.; Zhao, Y.; Gerhard, E.; Li, Y.; Yang, J.; Guo, J. Anti-Oxidant Anti-Inflammatory and Antibacterial Tannin-Cross-linked Citrate-Based Mussel-Inspired Bioadhesives Facilitate Scarless Wound Healing. *Bioact. Mater.* **2023**, *20*, 93–110.
- (30) Guo, J.; Tian, X.; Xie, D.; Rahn, K.; Gerhard, E.; Kuzma, M. L.; Zhou, D.; Dong, C.; Bai, X.; Lu, Z.; Yang, J. Citrate-Based Tannin-Bridged Bone Composites for Lumbar Fusion. *Adv. Funct. Mater.* **2020**, *30*, 2002438.
- (31) Zhao, Y.; Li, J.; Liu, L.; Wang, Y.; Ju, Y.; Zeng, C.; Lu, Z.; Xie, D.; Guo, J. Zinc-Based Tannin-Modified Composite Microparticulate Scaffolds with Balanced Antimicrobial Activity and Osteogenesis for Infected Bone Defect Repair. *Adv. Healthcare Mater.* **2023**, *12*, No. e2300303.

- (32) Dekoninck, S.; Blanpain, C. Stem Cell Dynamics, Migration and Plasticity during Wound Healing. *Nat. Cell Biol.* **2019**, *21*, 18–24.
- (33) Guerrero-Juarez, C. F.; Dedhia, P. H.; Jin, S.; Ruiz-Vega, R.; Ma, D.; Liu, Y.; Yamaga, K.; Shestova, O.; Gay, D. L.; Yang, Z.; Kessenbrock, K.; Nie, Q.; Pear, W. S.; Cotsarelis, G.; Plikus, M. V. Single-Cell Analysis Reveals Fibroblast Heterogeneity and Myeloid-Derived Adipocyte Progenitors in Murine Skin Wounds. *Nat. Commun.* **2019**, *10*, 650.
- (34) Cangkrama, M.; Wietecha, M.; Werner, S. Wound Repair, Scar Formation, and Cancer: Converging on Activin. *Trends Mol. Med.* **2020**, *26*, 1107–1117.
- (35) Chang, M.; Nguyen, T. T. Strategy for Treatment of Infected Diabetic Foot Ulcers. *Acc. Chem. Res.* **2021**, *54*, 1080–1093.
- (36) Ono, M.; Masaki, A.; Maeda, A.; Kilts, T. M.; Hara, E. S.; Komori, T.; Pham, H.; Kuboki, T.; Young, M. F. CCN4/WISP1 controls cutaneous wound healing by modulating proliferation, migration and ECM expression in dermal fibroblasts via $\alpha 5\beta 1$ and TNF α . *Matrix Biol.* **2018**, *68–69*, 533–546.
- (37) Bai, X.; Zhao, G.; Chen, Q.; Li, Z.; Gao, M.; Ho, W.; Xu, X.; Zhang, X. Q. Inhaled siRNA Nanoparticles Targeting IL11 Inhibit Lung Fibrosis and Improve Pulmonary Function Post-Bleomycin Challenge. *Sci. Adv.* **2022**, *8*, No. eabn7162.
- (38) Shi, Y.; Wang, S.; Zhang, W.; Zhu, Y.; Fan, Z.; Huang, Y.; Li, F.; Yang, R. Bone marrow mesenchymal stem cells facilitate diabetic wound healing through the restoration of epidermal cell autophagy via the HIF-1 α /TGF- β 1/SMAD pathway. *Stem Cell Res. Ther.* **2022**, *13*, 314.
- (39) Geesala, R.; Bar, N.; Dhoke, N. R.; Basak, P.; Das, A. Porous Polymer Scaffold for On-Site Delivery of Stem Cells-Protects from Oxidative Stress and Potentiates Wound Tissue Repair. *Biomaterials* **2016**, *77*, 1–13.
- (40) Wang, T.; Li, W.; Zhang, Y.; Xu, X.; Qiang, L.; Miao, W.; Yue, X.; Jiao, X.; Zhou, X.; Ma, Z.; Li, S.; Ding, M.; Zhu, J.; Yang, C.; Wang, H.; Li, T.; Sun, X.; Wang, J. Bioprinted Constructs that Simulate Nerve-Bone Crosstalk to Improve Microenvironment for Bone Repair. *Bioact. Mater.* **2023**, *27*, 377–393.
- (41) Liu, X.; Wu, K.; Gao, L.; Wang, L.; Shi, X. Biomaterial Strategies for the Application of Reproductive Tissue Engineering. *Bioact. Mater.* **2022**, *14*, 86–96.
- (42) Baudequin, T.; Tabrizian, M. Multilineage Constructs for Scaffold-Based Tissue Engineering: A Review of Tissue-Specific Challenges. *Adv. Healthcare Mater.* **2018**, *7*, 1700734.
- (43) Chen, Z.; Xiao, L.; Hu, C.; Shen, Z.; Zhou, E.; Zhang, S.; Wang, Y. Aligned Lovastatin-Loaded Electrospun Nanofibers Regulate Collagen Organization and Reduce Scar Formation. *Acta Biomater.* **2023**, *164*, 240–252.
- (44) Eming, S. A.; Martin, P.; Tomic-Canic, M. Wound Repair and Regeneration: Mechanisms, Signaling, and Translation. *Sci. Transl. Med.* **2014**, *6*, 265sr6.
- (45) Wang, P.; Huang, S.; Hu, Z.; Yang, W.; Lan, Y.; Zhu, J.; Hancharou, A.; Guo, R.; Tang, B. In Situ Formed Anti-Inflammatory Hydrogel Loading Plasmid DNA Encoding VEGF for Burn Wound Healing. *Acta Biomater.* **2019**, *100*, 191–201.
- (46) Veith, A. P.; Henderson, K.; Spencer, A.; Sligar, A. D.; Baker, A. B. Therapeutic Strategies for Enhancing Angiogenesis in Wound Healing. *Adv. Drug Delivery Rev.* **2019**, *146*, 97–125.